Master Thesis

Phase formation and mechanical properties of AlMgB$_{14}$ thin films

carried out for the purpose of obtaining the degree of Dipl.-Ing., submitted at TU Wien, Faculty of Mechanical and Industrial Engineering, by

Erwin Peck, BSc

under the supervision of

Univ.Prof. Dipl.-Ing. Dr.mont. Paul Heinz Mayrhofer

and

Univ.Ass. Dipl.-Ing. Dr.techn. Alexander Kirnbauer, BSc

Institute of Materials Science and Technology, E308

Vienna, July 2022

I confirm, that going to press of this thesis needs the confirmation of the examination committee.

Affidavit

I declare in lieu of oath, that I wrote this thesis and performed the associated research myself, using only literature cited in this volume. If text passages from sources are used literally, they are marked as such.

I confirm that this work is original and has not been submitted elsewhere for any examination, nor is it currently under consideration for a thesis elsewhere.

I acknowledge that the submitted work will be checked electronically-technically using suitable and state-of-the-art means (plagiarism detection software). On the one hand, this ensures that the submitted work was prepared according to the high-quality standards within the applicable rules to ensure good scientific practice "Code of Conduct" at the TU Wien. On the other hand, a comparison with other student theses avoids violations of my personal copyright.

_____   _____
City and Date   *Signature*

Acknowledgements

I would like to express my sincerest gratitude to Univ. Prof. Dipl.-Ing. Dr.mont. Paul H. Mayrhofer for giving me the opportunity to write my thesis in his research group. Despite the difficult times, I could always rely on your professional guidance and supervision. Although I was very limited in time due to different factors in my life, you always had an open ear for me. I hope that our future interactions will take place in person.

I would especially like to thank my thesis adviser Alexander for his guidance, help and constant support during the whole research work, even though he was almost ten thousand kilometres away. Hopefully, our future cooperation remains as exciting as on the first day at our institute.

Special thanks go to all my colleagues at the research group, who were always supportive and understanding. Especially, to my roommates Michael, Balint, Alex, Rebecca and Barbara, for their support, the excellent Teamwork and the stimulating and interesting conversations.

Appreciation is also extended to the members of the Institute of Materials Science and Technology, E308, who taught me a lot in a very short amount of time. First and foremost, the correct handling of our machines.

I just want to say THANK YOU to all my friends and colleagues, who accompanied me during my journey at the TU Wien and of course to my family who always reminds me of what is important in life.

Finally, I would like to say a big thank you to my lovely girlfriend Lisa who has supported me through every stage of my life and of course to her family who have always been there for me.

Table of Contents

Abstract

AlMgB$_{14}$ is one of the most promising thin film materials for industrial use as protective coating for cutting tools and high-temperature components. Therefore, in this work, we use PVD to synthesize AlMgB$_{14}$ coatings at substrate temperatures ranging from 300 to 600 °C to get detailed information about the morphology, and mechanical properties of the prepared samples.

Independent on the applied substrate temperature (T$_s$), the coating exhibited an amorphous structure growing with a rate of 52 to 60 nm/min. The hardness and Young's modulus increase with increasing substrate temperature from 29.3 ± 1.6 GPa to 35.3 ± 1.0 GPa and from 373 ± 17 GPa to 413 ± 8 GPa respectively. All the coatings exhibit residual stresses varying between -2 GPa and -3 GPa and are thus almost independent of the substrate temperature. As the substrate temperature increases, the fracture toughness also increases, exhibiting a value of 3.72 ± 0.46 MPa√m for T$_s$ = 300 °C and a force of 250 mN, and 5.15 ± 0.22 MPa√m for T$_s$ = 600 °C, respectively.

After analyzing the properties of the layers in their as deposited state, annealing tests were carried out with the most promising sample (T$_s$ = 600 °C). Upon vacuum annealing the samples between 850 and 1050 °C for 20 min, the hardness as well as the indentation modulus show a slight increase of 1 GPa and 50 GPa, respectively, but remained amorphous.

Kurzfassung

$AlMgB_{14}$ ist eines der vielversprechendsten Dünnschichtmaterialien für den industriellen Einsatz als Schutzschicht für Schneidwerkzeuge und Hochtemperaturkomponenten. Daher verwenden wir in dieser Arbeit physikalische Gasphasenabscheidung (PVD), um $AlMgB_{14}$-Beschichtungen bei Substrattemperaturen von 300 bis 600 °C zu synthetisieren und detaillierte Informationen über die Morphologie und die mechanischen Eigenschaften der hergestellten Proben zu erhalten [1].

Unabhängig von der angewandten Substrattemperatur (T_s) wies die Beschichtung eine amorphe Struktur auf, die mit einer Wachstumsrate von 52 bis 60 nm/min wuchs. Mit zunehmender Substrattemperatur steigt die Härte von 29.3 ± 1.6 GPa auf 35.3 ± 1.0 GPa und der Elastizitätsmodul von 373 ± 17 GPa auf 413 ± 8 GPa. Alle Beschichtungen weisen Eigenspannungen auf, die zwischen -2 und -3 GPa schwanken und nahezu unabhängig von der Substrattemperatur sind. Mit steigender Substrattemperatur nimmt auch die Bruchzähigkeit zu, die bei T_s = 300 °C und einer Kraft von 250 mN einen Wert von 3,72 ± 0,46 MPa√m und bei T_s = 600 °C einen Wert von 5,15 ± 0,22 MPa√m aufweist.

Nach der Analyse der Eigenschaften der Schichten in deren Herstellungszustand wurde die vielversprechendste Probe (T_s = 600 °C) im Bereich zwischen 850 und 1050 °C vakuumgeglüht für 20 min. Nach dem Glühen zeigte diese Probe weiterhin eine amorphe Struktur aber eine um ca. 1 GPa höhere Härte und einen um ca. 50 GPa höheren Elastizitätsmodul.

List of Figures

List of Tables

List of Abbreviations and Symbols

Ar .... $Argon$

c .... $length\ of\ the\ radial\ cracks$

CVD .... $Chemical\ Vapor\ Deposition$

d .... $distance\ between\ lattice\ plane,\ film\ thickness$

D .... $substrate\ thickness$

E .... $young's\ modulus$

E* .... $normalised\ energy$

E_{Ar+} .... $kinetic\ energy\ of\ the\ argon\ ion$

E_S .... $young's\ modulus\ of\ the\ substrate$

FEGSEM .... $field\ emission\ gun\ scanning\ electron\ microscopy$

H .... $hardness$

K_c .... $fracture\ toughness$

M_{Ar+} .... $mass\ of\ the\ argon\ ions$

M_{TA} .... $mass\ of\ the\ target\ atom$

n .... $integer$

P .... $peak\ indentation\ load$

PVD .... $Physical\ Vapor\ Deposition$

R .... $bending\ radius$

SEM .... $Scanning\ electron\ microscopy$

SZM .... $structure\ zone\ model$

t* .... $film\ thickness$

T* .... $generalised\ temperature$

U_{TA} .... $binding\ energy\ of\ the\ target\ atom$

XRD .... $X\text{-}Ray\ diffraction$

Y .... $sputter\ yield$

α .... $constant\ of\ the\ tip\ geometry$

$\alpha\text{-}Al_2O_3$ .... $single\ crystal\ \alpha\text{-}aluminium\ oxide$

γ-Iron .... $austenite\ iron$

θ .... $diffraction\ angle$

λ .... $wavelength$

ν .... *Poission number*

σ ....*residual stresses*

σ_{if-f}.. *interface energy between two films*

σ_f ....*surface energy of the film*

σ_{if} .... *interface energy between substrate and film*

σ_s .... *substrate surface energy*

1 Introduction

In the field of materials science many different aspects regarding the properties of materials have to be taken into account. The most important properties are mechanical properties like hardness, toughness, and yield strength. But also, high-temperature properties such as oxidation resistance and phase stability as well as tribological properties are very important for many applications. To increase the performance of components one can, enhance the properties of the bulk material itself, or improve specifically the properties of the surface or surface near regions through surface engineering and technology [1]. This can be achieved by thermochemical methods e.g., nitriding or surface hardening or by applying a coating with the desired properties on the surface of the component or tool. One of the most commonly used techniques to apply coatings is physical vapor deposition (PVD)[2]. Thereby, protective coatings such as TiN [3], (Ti,Al)N [4], or more complex material systems e.g. (Ti,Al,Ta)N [5], [6], (Cr,Al,Si)N [7] or even coatings based on the high-entropy concept [8–11] are investigated and applied. In 1970 a newly developed material namely $AlMgB_{14}$ was first produced by V.I. Matkovich and J.Economy at the Carborundum Company [12]. The resultant boride is a very attractive material due to its extreme hardness [13], its low coefficient of friction value [14], low density [12] and its high thermal stability [15]. These properties make $AlMgB_{14}$ a very interesting material system also for PVD applications. In previous studies it was shown that $AlMgB_{14}$ coatings can be synthesized by DC magnetron sputtering [16,17], RF magnetron sputtering [18], and by pulsed laser deposition [19]. In order to obtain further information on the phase formation and mechanical properties, $AlMgB_{14}$ films on silicon, sapphire, austenite, alumina substrates, and low-alloyed steel foil, were magnetron sputtered using a single stoichiometric $AlMgB_{14}$ target. The main variable was the substrate temperature, which prevailed during the deposition process and was varied from 300 to 600 °C in steps of hundreds.

For this purpose, the hardness was determined by nanoindentation, the residual stresses by non-contact profilometry, the fracture toughness by cube-corner indentation and scanning electron microscopy (SEM), the layer thickness by SEM and the morphology also by SEM and X-ray diffraction.

In addition, an attempt was made to produce a crystalline structure from the previously produced $AlMgB_{14}$ layer (T_s = 600 °C) by means of annealing tests. For this purpose, the sample was annealed for 20 min at temperatures of 850, 900, 950, 1000, and 1050 °C in a vacuum annealing furnace and then examined by XRD. After these annealing treatments, the hardness and the Young's modulus of the film was determined again.

2 Methods

2.1 Deposition Technologies

For materials of any kind, fatigue resistance, hardness, and corrosion resistance are very important. Therefore, applying a coating to enhance the properties of a surface is often used to increase the lifetime of many different components. A wide variety of processes are used in industry to produce thin films, one of the most popular and widely used is physical vapor deposition (PVD). Chemical vapor deposition (CVD) should also be mentioned, as it is one of the most popular coating technologies along with PVD. The main difference between the two is the vapor generation process, which, as the names suggest, is either physical or chemical [20].

2.1.1 Physical Vapor Deposition

PVD technologies can basically be divided into three different processes which are, evaporation, ion plating, and sputtering. The coatings investigated in the framework of this thesis were synthesized using magnetron sputtering. Any PVD-based coating technology involves three main process steps. The first step is the physical transfer of a material from the solid or liquid state to the vapor state. This is also the reason why this is called PVD. The second step of any PVD process is the transport of the gaseous species to the parts which should be coated also called substrate. And the last step, is the condensation of the material on the substrate and the thereby initiated film growth.

2.1.1.1 Sputtering Process

The mechanism of sputtering is based on momentum transfer. This means that the impulse in the collision of two particles is preserved. The impact of species is responsible for the ejection of atoms from the material to be vaporized, the so-called target. Such a process is called sputtering. If no compound layer should be formed and only elements from the target should form the desired film, the working gas should be inert and mostly argon (Ar) is used. There are several reasons why Ar is the preferred choice including its prize, availability, as well as stable process conditions. Via the formation of a plasma, the thereby available positively charged Ar-ions are attracted to the target material by applying a high negative potential to it. The high energetic impact triggers a collision cascade process, which, if energetic enough allows atoms to leave the material (sputtered atoms).
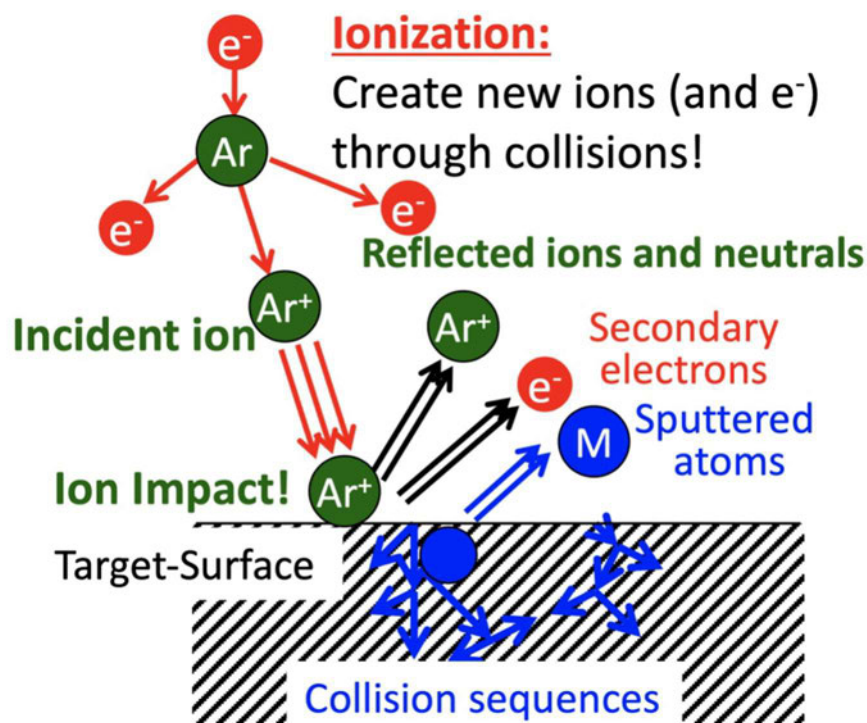

Figure 1: Sputtering: ionisation, movement to the cathode, impact of ions and sputtering of atoms [21]

The plasma is ignited by using an electric field between the target (cathode) and the vacuum chamber (anode). The originated electrons collide with argon atoms, leading to further ion generation. These ions are, due to a negative potential, accelerated towards the target surface, where target atoms are ejected. The impact of the ion can cause different reactions. First of all, the ions themselves can be reflected, target atoms can be ejected, and secondary electrons can be generated. These lead to a collision-cascade and in further consequence to a self-sustaining plasma and therefore a stable sputtering process. The sputter yield Y was defined to describe the efficiency of the sputtering process. It describes the ratio of bombarding ions to sputtered atoms and is defined as

$$Y = \alpha * \frac{M_{Ar+} + M_{TA}}{(M_{Ar+} + M_{TA})^2} * \frac{E_{Ar+}}{U_{TA}} \tag{1}$$

where α is the angle of incidence, M_{Ar+} is the mass of the argon ions, M_{TA} is the mass of the target atom, E_{Ar+} is the kinetic energy of the argon ions and U_{TA} is the binding energy of the target atom. Normally, the sputter yield for an efficient sputter process has a value between one and three. A schematic of the described process is illustrated in Figure 1.

In terms of energy loss, sputtering is very inefficient because 95% of the energy produced by the colliding ions, transforms to thermal energy and leads to heating up the target and secondary electrons. Therefore, it is important to cool the target constantly [20].

2.1.1.2 Magnetron Sputtering

The advantage of magnetron sputtering (see Figure 2) is that there is an outer and an inner ring-shaped magnetic pole behind the target, which are polarized in opposite directions. Due to the polarity of the said magnetic poles, a magnetic field is created between them. The magnetic field and the applied electric field bundle the electrons above the target and the electrons are moving in a circular movement over the target. This is the reason for the typical erosion of the target during magnetron sputtering, whose area is also called racetrack, shown in blue in Figure 2. The electron density is increased and therefore, more frequent collisions occur, which in turn leads to the multiple formation of ions. Therefore, the sputtering yield Y can be increased while maintaining a low overall deposition pressure.

The latter is advantageous as thereby fewer gas scattering processes take place especially for the sputtered species during their flight to the substrate material. Thus, they arrive with higher energy for example.
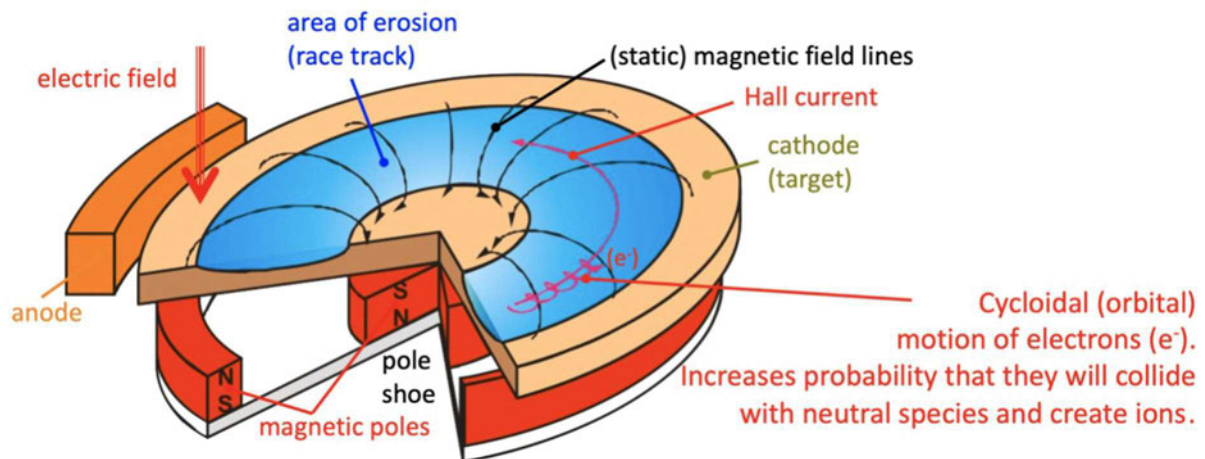

Figure 2: Magnetron Sputtering [21]

2.1.1.3 Substrate Bias Voltage

By applying a negative voltage (typically -50 to -200 V) to the substrate holder, the so-called bias voltage, the flow of ions towards the substrate(s) is increased. These impinging ions bring further energy to the substrate surface and this in turn favors the mobility of the adatoms and can thus improve the properties of the layer, such as density or step coverage.

For the substrate surface pre-preparation (before the actual deposition process), an increased pulsed bias voltage is applied to the substrates. Thereby, Ar-ions attracted to the substrate surface are energetic enough to initiate sputtering events there, which removes surface contaminants, this process is called substrate etching.

2.1.1.4 Film Growth

The layer growth has a decisive influence on the properties of the coating, such as crystalline structure, chemical composition, and growth morphology. Therefore, it is of great interest to have as much information as possible about this. It is even more important to know how the growth of the coating can be influenced by the deposition parameters, like gas pressure, substrate temperature, or substrate bias voltage, to improve the properties.
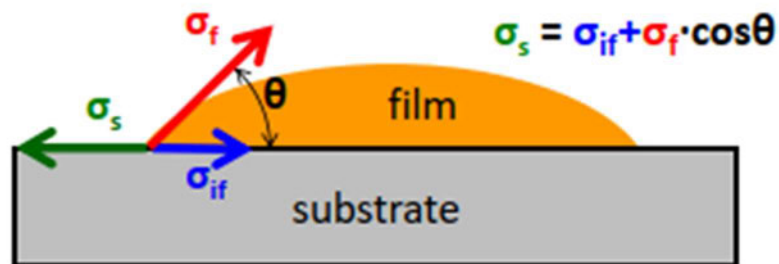

Figure 3: Equilibrium of the energies at the contact of film and substrate [21]

Depending on the relationship of the surface energy that occurs when an adatom comes into contact with the substrate, as shown in Figure 3, different growth modes occur.

σ_s is the substrate surface energy, σ_f is the surface energy of the film and σ_{if} is the interface energy between the substrate and the film.

Based on the equilibrium formula,

$$\sigma_s = \sigma_{if} + \sigma_f * \cos\theta \qquad (2)$$

and comparing the interface energy between substrates and film σ_{if} and the interface energy between two films σ_{if-f}, the following classification can be made:

- **Layer-by-layer growth (Frank-van der Merwe)**: The growth is two-dimensional, i.e. a complete layer is formed on the surface before the next layer grows. The film atoms adhere to the substrate rather than to another atom. If $\sigma_s > \sigma_{if} + \sigma_f$,and $\sigma_f > \sigma_{if-f}$ are satisfied, then layer by layer growth occurs (see Figure 4 left).

- **Island growth (Vollmer-Weber):** Growth comes from droplet-shaped nuclei, or islands. This three-dimensional type of growth occurs when σ_s is smaller than $\sigma_{if} + \sigma_f$.This means that the adatoms stick to each other rather than to the surface (see Figure 4 middle).

- **Mixed growth (Stranski-Krastanov):** Initially, the structure is layered and then it changes to island growth, i.e., it is a mixture of the two growth types listed above. This happens when $\sigma_s > \sigma_{if} + \sigma_f$ and $\sigma_f < \sigma_{if-f}$ applies (see Figure 4 right).
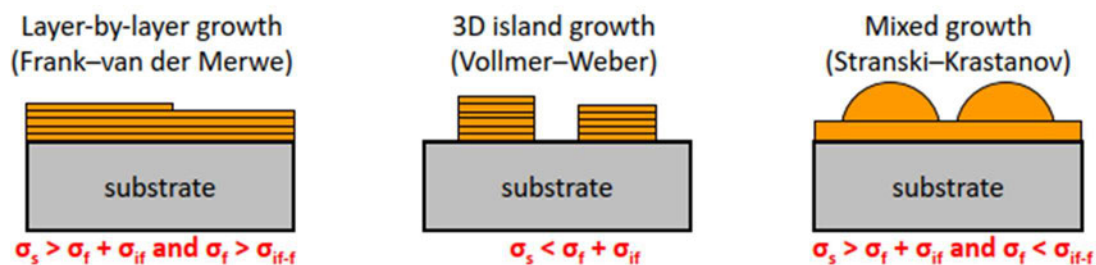

Figure 4: Illustration of layer-by-layer (left), island (middle), and mixed growth (right) [21]

As mentioned before, one wants to control the properties of the layer by means of deposition parameters. An important tool for this is the structure-zone diagram, which has been improved and refined over the years. Movchan and Demchishin started in 1969 with a structure zone model (SZM), which is divided into three areas and depends on the homologous temperature. The homologous temperature is defined as the substrate temperature divided by the melting temperature of the layer [22]. Thornton (1977) and Messier (1984) improved this diagram by making it dependent on pressure and energy. This resulted in a new fourth zone, between the first and second zone, called transition zone (zone T) [23], [24].

One of the most used SZM (see Figure 5) is that by Andre Anders [25], who made the three-dimensional diagram dependent on the generalised temperature T*, the normalised energy E*, and film thickness t*. T* is the sum of the homologous temperature and the characteristic temperature of the heated region, which depends on the energy of the impinging particles and thus also on the bias voltage of the substrate.

E* takes into account the characteristic energy of the material, the kinetic energy of the impacting particles, the ratio of the masses of the impacting ions and atoms to those already on the surface. The kinetic energy depends on the gas pressure and the momentum transfer is reflected in the mass ratio. And finally, the film thickness, which illustrates that if the E* is too high, the film thickness can decrease due to ion etching.

In zone 1, the shading effect is predominant. This means that due to the low energy and the low temperature, the adatoms remain at their point of impact and move no longer. This leads to grains growing upwards in a cone shape starting from a nucleon and to areas where no adatoms can reach. This leads to a porous layer with a high dislocation density. In the transition zone (zone T), the diffusion effect starts due to the higher energy and temperature, which in turn compensates for the shadowing effect and closes the holes that have formed. Therefore, densely packed fibrous grains are formed.

Zone 2 is determined by the diffusion effect, which leads to the growth of thicker and thicker columns as the temperature increases.

In zone 3, the mobility of the particles is so high that they can diffuse into the mass and recrystallisation occurs. This leads to epitaxial growth.

At energies exceeding this range, the layer is finally eroded and the ion etching zone is reached [25].
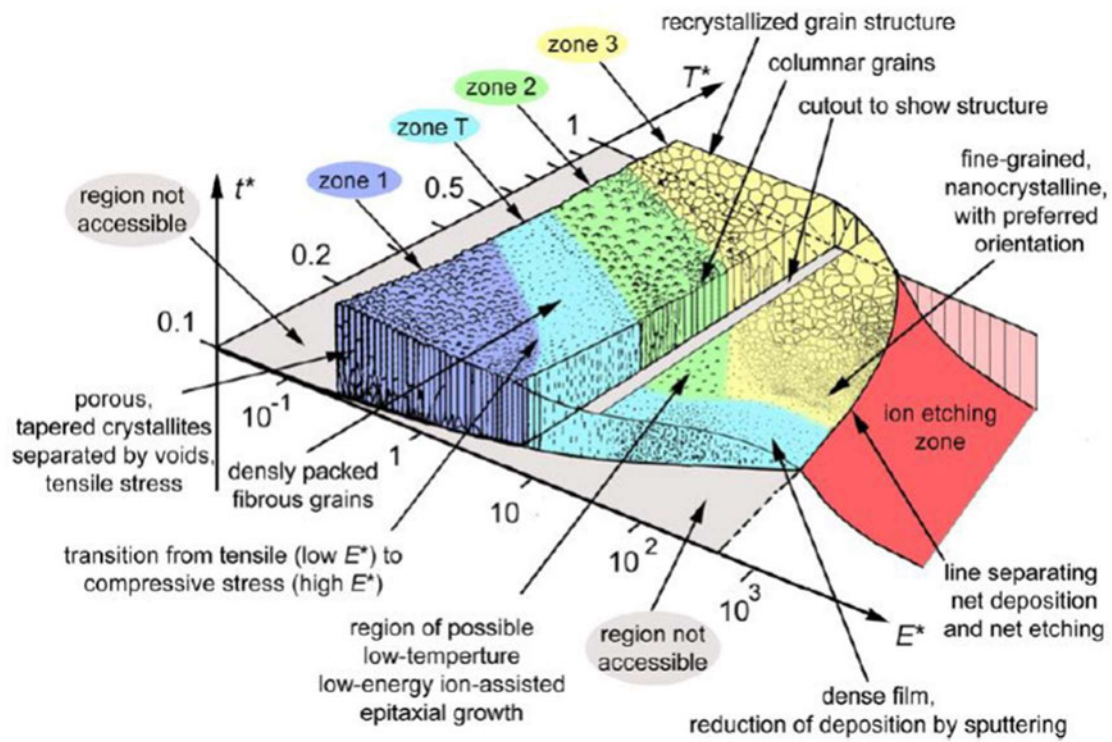
Figure 5: Structure Zone diagram by Anders [25]

2.1.2 Experimental Procedure

In order to make coating processes and results reproducible, it is essential that all parameters and processes are meticulously documented.

Before the actual coating can be started, some preparations must be made. Each substrate to be coated must be cleaned beforehand (see 2.2.1) and placed in the substrate holder and the target must be bonded to the water-cooled cathode with indium (high thermal and electrical conductivity) beforehand. If these precautions have been taken, they can be installed in the coating system.

The deposition facility, more precisely a Leybold Heraeus Z400 laboratory PVD system, can operate a 3-inch cathode, which is water cooled and the substrates can be heated up to 700 °C. The cathode can be used for the deposition of the substrate. The distance between substrate surface and target can be adjusted up to a distance of 39 mm.

After cleaning the coating chamber with a vacuum cleaner and ethanol, the first step is to clean the target from impurities on the surface and remove oxides, which are formed on the surface before in atmosphere, which means the system is operated without substrates with the later coating parameters for a few minutes. This is to remove further impurities and to apply a layer of the used material system in the chamber to avoid contamination from previous coatings. After the pressure of the system has been brought below a value of 10^{-4} Pa absolute pressure, which can be optimized with liquid nitrogen in the cooling trap, and thus a sufficiently good vacuum has been established and the desired substrate temperature has been reached, the ion etching process can be started. This process is necessary to clean the surface of the substrates from contaminations or deposits and takes about 15 minutes. A bias voltage of -150 V is applied to the substrate holder in pulsed mode, which means that the voltage is pulsed with a frequency of 150 kHz and a pulse width of 2496 ns. Even if there is a good high vacuum in the chamber (10^{-4} Pa) it takes only 2 seconds for the remaining air or oxygen to form a monolayer on the substrates. Therefore, it is important that the transition from etching to deposition is fast and mild. This soft cross-over is made by igniting the sputtering plasma with the shutter closed and the coating parameters, such as argon flow (for reactive deposition, which is not used here, also the nitrogen flow or oxygen flow for example), bias voltage are already set towards the end of the etching process. When the shutter is opened, the deposition process begins.

2.2 Material System

The material system aluminium magnesium boride $AlMgB_{14}$ has been of importance in research in recent decades. The reasons for this are its good mechanical properties, such as its high strength, hardness and durability and a very low coefficient of friction. Previous studies [14], [15] have already investigated and documented these properties. This work is intended to reproduce already known measurements and will include other properties and measurements that have not yet been published.

It all started with contaminated boron. In 1970, Matkovich and Economy heated a mixture of aluminium borides to $1000 - 1400$ °C. The boron in the mixture was contaminated with magnesium. Because of this, small $AlMgB_{14}$ crystals could be extracted. Further investigations revealed that $AlMgB_{14}$ is an orthorhombic crystal structure with cell dimensions of a = 10.313 Å, b = 8.115 Å, and c = 5.848 Å and four icosahedral B12 units per unit cell. [12] The unit cell is composed of 4 B_{12}-icosahedra, 8 boron atoms, 3 magnesium atoms, 3 aluminium atoms and, 2 vacancies as shown in Figure 6 [26].
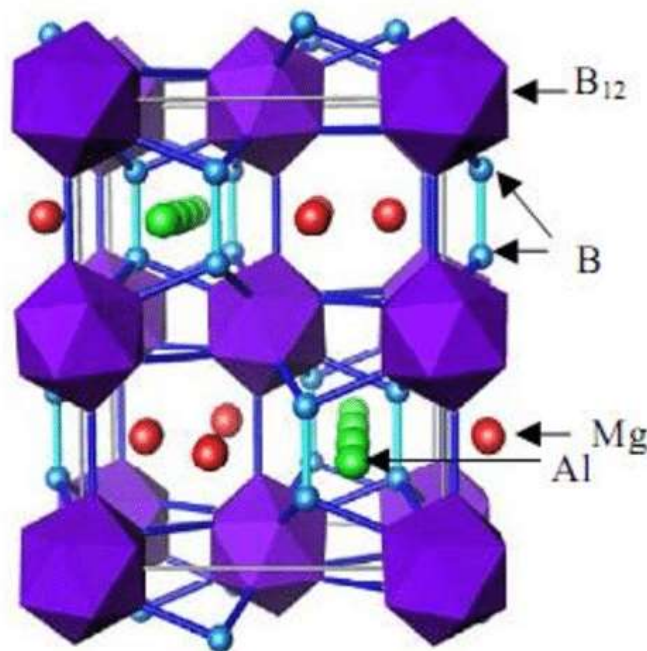

Figure 6: Unit cell of $AlMgB_{14}$ [26]

2.2.1 Substrates

The substrate is the material on which the layer is applied with a size of 10 x 10 mm or 20 x 7 mm. Before using the substrates, they were all, excluding sapphire, ultrasonically cleaned in a bath of ethanol for 5 minutes and those contaminated with adhesive were also cleaned with acetone for 5 minutes.

Silicon

Single-crystalline silicon substrates are usually used due to their advantageous properties. The silicon wafer was cut in (100) orientation and trimmed to a size of 20 x 7 mm. They are also excellent for investigating the cross section of the coating in a scanning electron microscope. Another advantage is that the single-crystalline silicon provides only one significant peak in X-Ray diffraction (XRD), which is typically not interfering with the reflexes of most of the coatings prepared in our lab.

Sapphire

Single crystal α-aluminium oxide (α-Al_2O_3) or also named sapphire was used as the substrate material for the coatings which have been investigated for their hardness, stresses, and for the annealing tests because they are not reacting with the coating even at temperatures above 1000 °C. The orientation of the substrate is in the direction of the R-plane (1-1 0 2). The reference pattern of α-Al_2O_3 substrate is shown in Figure 7.
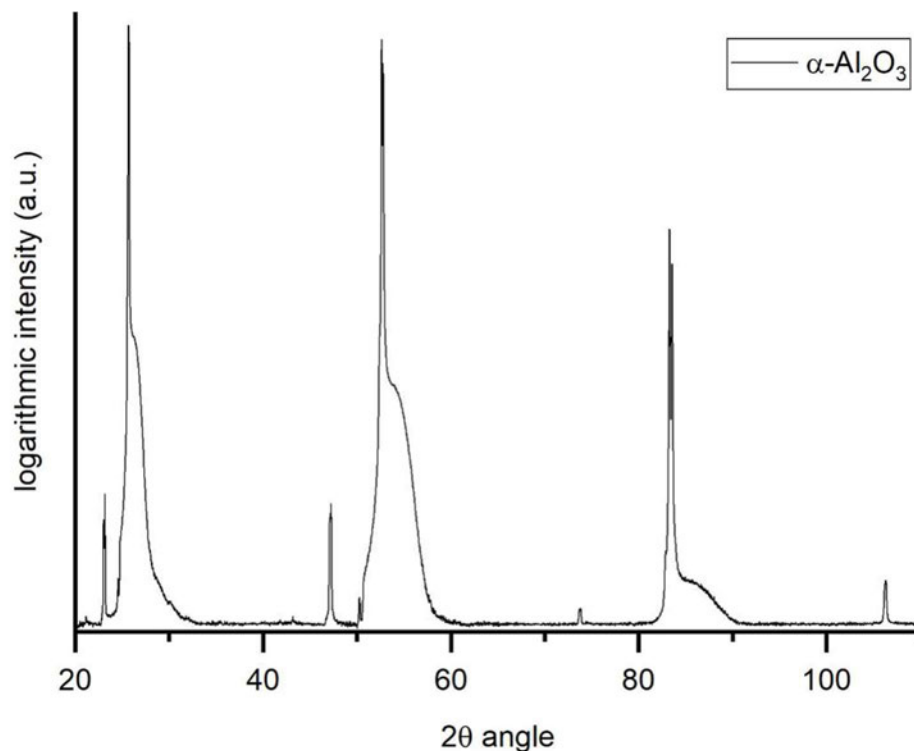

Figure 7: XRD reference pattern of α-Al_2O_3 substrate

13

Austenite

Austenite (γ-Iron) substrates that have been previously polished are used to investigate the adhesion of the coating regarding its possible application. The size of the substrates is 20 x 7 mm.

Iron foil

A 0.025 mm thick iron foil is used as a substrate to allow for a powder production of the deposited coatings.

For this purpose, a 3" substrate holder is covered with the foil and coated as usual, after the deposition, the iron foil is dissolved using hydrochloric acid and the free-standing coating material is ground to a powder with a ceramic mortar.

2.3 Analysis

After the successful coating process, it is important to examine the produced coatings for a variety of their properties. Different measurement methods were used for this purpose, which are described in more detail below.

2.3.1 X-Ray Diffraction (XRD)

X-Ray diffraction is a technique which is commonly used to get detailed information about the crystal structure and grain size of various materials. Basically, XRD focusses on the interaction between the X-rays and the investigated sample. At first, a sample is placed and later illuminated with an X-ray beam. The diffraction takes place when the incident beam hits the lattice planes of the sample in different angles. At this point a certain equation (Bragg's law) is used to analyze the correlation between the diffraction angle (θ), the distance of the lattice plane (d) and the wavelength (λ). The equation mentioned is called the Bragg's law [27], and the graphical derivation is shown in Figure 8:

$$n * \lambda = 2 * d * sin(\theta) \qquad (3)$$

In 1915 Sir William Henry Bragg and Sir William Laurence Bragg won the Nobel prize for being first in determining the crystal structure by using the X-Ray diffraction.

The order of diffraction is described by the integer n. By solving the Bragg equation with a given wavelength (λ) of the incident beam, the diffraction angles of the XRD peaks (θ) of certain lattice planes can be derived. [28]
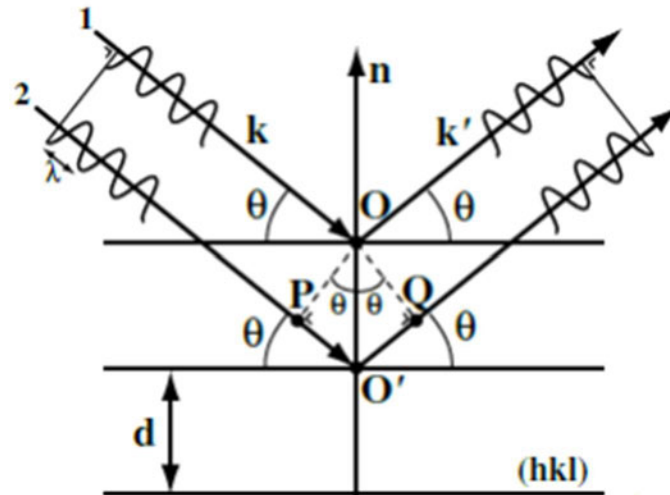
Figure 8: Illustration of constructive interference of X-rays and visualization of the way to get the Bragg's law [29]

2.3.2 In-Situ X-Ray Diffraction

In-situ XRD basically works on the same principle as ordinary XRD except that it is a sequential series of measurements while the sample is heated in a vacuum. More precisely, as shown in Figure 9, a predefined temperature profile is run through, and a measurement is taken at each horizontal when the temperature is constant. In this way, changes in the structure and microstructure can be illustrated as a function of temperature.
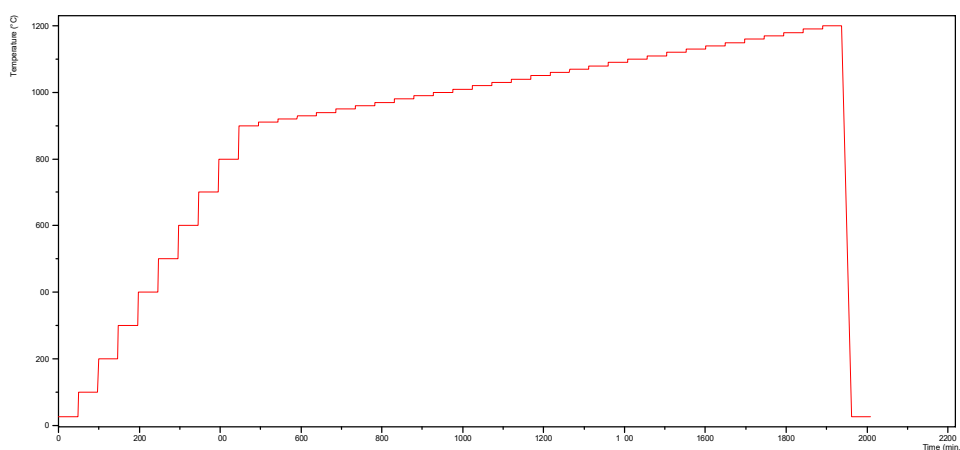

Figure 9: Temperature curve of the measurement of AlMgB$_{14}$

16

2.3.3 Nanoindentation

Nanoindentation is a commonly used method to test the mechanical properties such as hardness and indentation modulus of thin films. This technique can furthermore be used to determine properties like creep, fracture toughness and yield stress at the nano level. Another advantage is that this method does not necessarily require a high-quality microscope for the measurements of the indentation's impression because the contact area is measured with the indenter geometry and the depth of indentation. This measurement is visually illustrated in the load displacement curve (shown in Figure 10).

Nanoindentation is adequate for testing thin films and bulk materials, because it can limit the indentation depth to reduce the substrate effects. In the course of this research, a Berkovich indenter tip was used on a UMIS II nano-indenter and the measurement was carried out using the software IBIS II and evaluated according to the method of Oliver and Pharr [30]. It should be noted that the geometry of the tip changes with continuous use and this change must be considered in the calculation by means of the area function. It is recommended that the area function is regularly re-determined. It should also be ensured that the penetration depth of the measurement does not exceed 10 percent of the coating thickness.
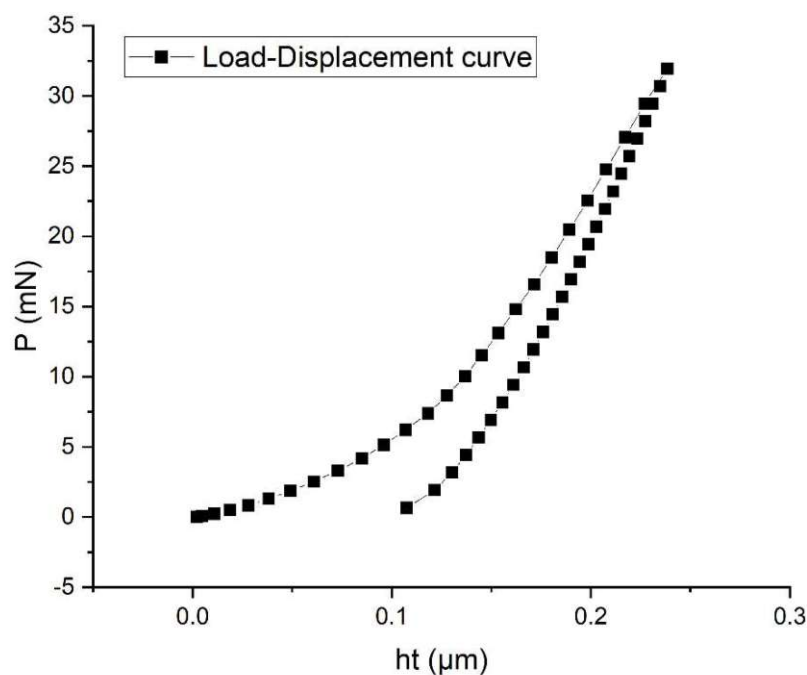

Figure 10: Load-Displacement curve of AlMgB$_{14}$ on sapphire with T$_s$ = 300 °C

17

2.3.4 Cube-Corner Indentation

The cube corner identification method is very similar to nanoindentation, it is performed on the same measuring device and with the same software. Only a different tip is used, the cube corner tip. Its sharper geometry is used to create cracks at the edges of the indentations in the layer. This measurement process is repeated for a previously defined range of forces. All the indentations are then visualized by SEM and after checking the cracks (which should always be only at the corners of the indentations), they are measured.

This method was first published by Pharr [31] and is used to determine the fracture toughness of coatings. The fracture toughness K_c can be determined with the help of

$$K_c = \alpha \left(\frac{E}{H}\right)^{1/2} \left(\frac{P}{c^{3/2}}\right), \qquad (4)$$

which was defined by Lawn, Evans, and Marshall [32].

Where α is a constant of the tip geometry, P is the peak indentation load, c is the length of the radial cracks (measured as in Fig. 11) and, E and H are the Young's modulus and hardness, respectively, which have already been determined by nanoindentation.
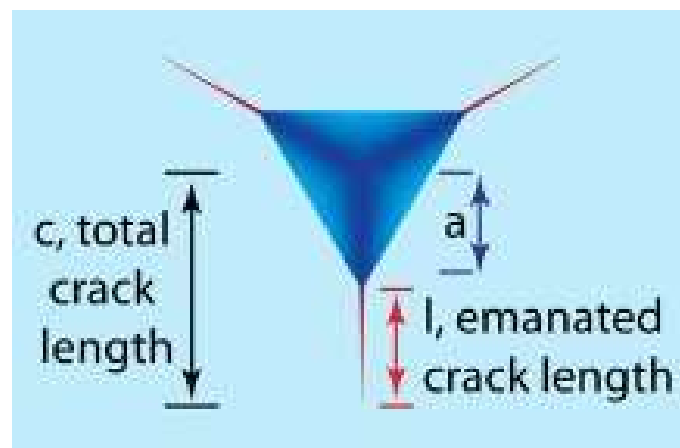

Figure 11: Geometric parameter (a, l, and c) for equation (4) [33]

2.3.5 Vacuum Annealing

The temperature resistance of materials and their surface coatings is a very important property because it is often required by the application, e.g., engines, machine tools or turbines. Therefore, it is of interest that coatings are heated to a high temperature and then examined for changes in their structure and material properties. For this purpose, a vacuum annealing furnace is used, in which the samples are heated in a vacuum (in the range of high 10^{-4} Pa) with an individually programmable heating cycle. The annealed samples are investigated similarly as the as-deposited ones.

2.3.6 Scanning Electron Microscopy (SEM)

A scanning electron microscope generates images by projecting and scanning focused electron beams over a sample surface. SEM is considered the most prevalent technique in microscopy because it is easy to handle, and the preparation of the samples is rather easy. The basic principle of this method relies on an interaction between the electrons in the beam and the sample, and due to that the electrons produce a variety of signals which can be used to derive information about the surface structure and composition.

The source of electrons, an electron detector, a sample chamber, a suitable display, and a column from top to bottom make up the main components of a SEM. The process starts with the production of electrons at the top of the mentioned column. The electrons pass down the column through different lenses and produce a more focused beam which strikes the sample's surface and with various signals produce an image of the surface. [34]

2.3.7 Non-Contact Profilometry

No-contact profilometry is based on chromatic confocal technology, where the wavelength of light is used to measure differences in height. Through a series of lenses (see Fig. 12, number 2) the different wavelengths of white light (Fig. 12, number 3) are focused to different heights, this is also called the optical aberration effect. As can be seen in Figure 12, the surface of the sample (Fig. 12, Nr. 1) is only in the focus of the middle (green) wavelength and therefore only this is reflected and measured by the spectrometer (Fig. 12, Nr. 4). This method has the advantage that it can be carried out very quickly and does not require any mathematical calculations. Thus, 3D surfaces can be determined with an accuracy of 0.1 nm and thus the roughness of the surface or the deflection can be measured and subsequently the residual stresses can be determined by means of the Stoney equation [21], [35].
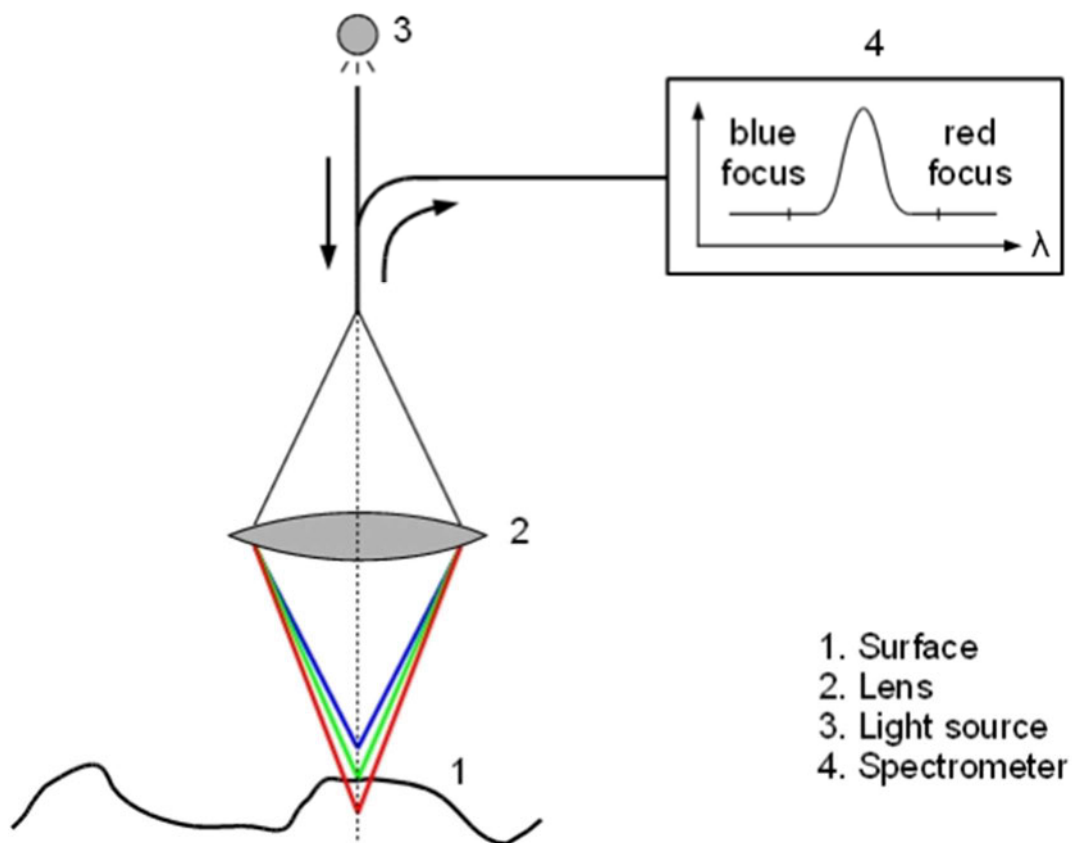
Figure 12: Principle of chromatic white light measurement [36]

3 Results and Discussion

In this chapter, the results of the investigations are presented, divided into the morphology and the mechanical properties. More specifically, for the morphology, the results of the field emission gun scanning electron microscopy (FEGSEM) and the results of the XRD are presented, and for the mechanical properties, the results of the nanoindentation, cube-corner indentation and non-contact profilometry measurements are presented.

3.1 Morphology

3.1.1 As-Deposited films

In order to identify the morphology of the coatings and possible differences due to the parameter variations of the deposition process, the fracture cross-section of coatings deposited on silicon substrates was visualised using FEGSEM.

To determine the influence of the substrate temperature on the structure of the coating and the layer growth rate, four coating processes were carried out at temperatures ranging from 300 to 600 °C in 100 °C steps, with all other parameters remaining constant. The remaining parameters of the non-reactive and current-controlled process were the target current of 0.75 A, the Ar flow rate of 35 sccm, a process pressure of 0.4 Pa, and a deposition time of 60 minutes and using floating potential at the substrates throughout the process.

The coating produced at the lowest substrate temperature T_s (300 °C, Fig. 13a) has a thickness of 3.115 μm and thus a deposition rate of 51.9 nm/min, the second coating (T_s = 400 °C, Fig. 13b) has a thickness of 3.595 μm and thus a coating rate of 59.9 nm per minute, layer 3 (T_s = 500 °C, Fig. 13c) has a thickness of 3.182 μm and a rate of 53 nm/min and the last layer (T_s = 600 °C, Fig. 13d) was 3.483 μm thick and thus had a rate of 58 nm/min. All layers (a-d in Fig. 13) have approximately the same thickness and thus all processes had a similar deposition rate. Also, clearly visible in the cross-sectional SEM images (Fig. 13) is that the layers have a feature-less growth morphology suggesting that they are amorphous.
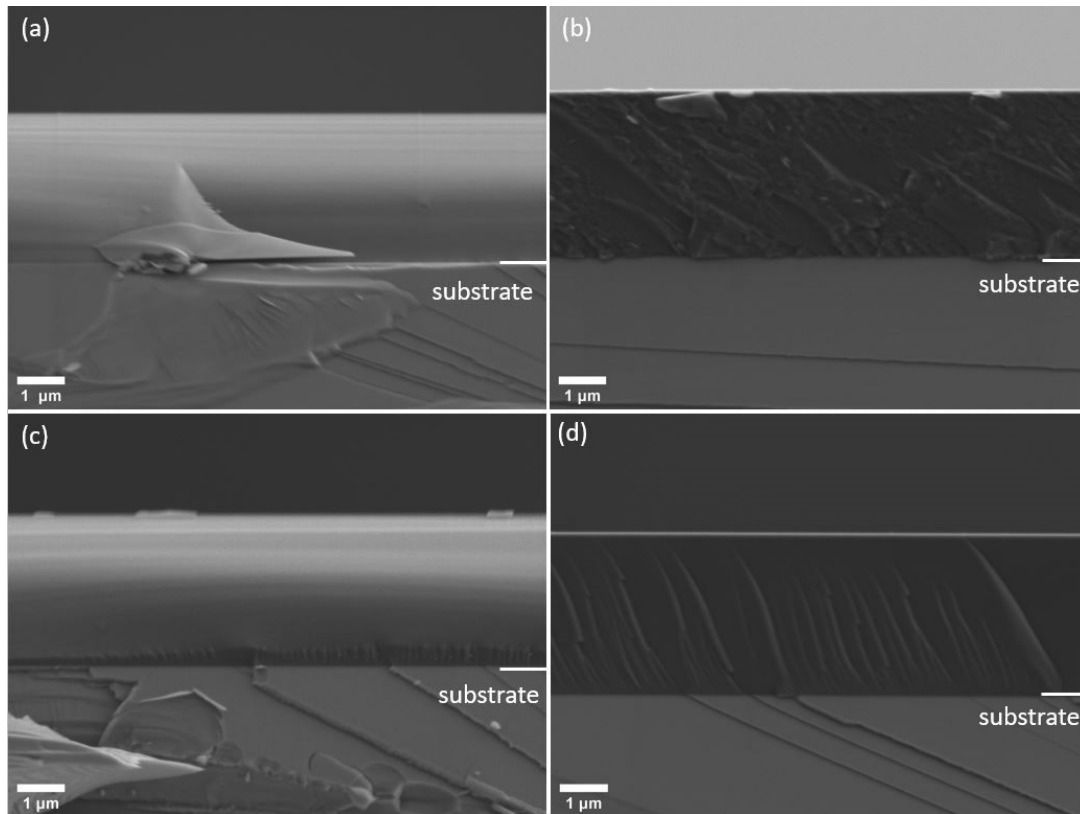
Figure 13: Cross-section FEGSEM images of AlMgB$_{14}$ on sapphire substrate with (a) 300 °C, (b) 400 °C, (c) 500 °C and (d) 600 °C substrate temperature

Confirmation that the structure is amorphous was provided by the XRD patterns (Fig. 14) of the AlMgB$_{14}$ coatings of the four layers mentioned above. All four measurements gave similar results, which was expected as only crystalline structures are detected by XRD and the coatings at the substrate temperatures 300 °C (blue line in Fig. 14), 400 °C (green line, Fig. 14), 500 °C (orange line, Fig. 14), and 600 °C (red line, Fig. 14) are all amorphous. Only the significant peaks for the silicon substrate are visible in Figure 14 at a 2θ-angle of 33.1°, the (200) diffraction of the Cu-K$_{\alpha1}$ and Cu-K$_{\alpha2}$ radiations can be seen, as well as the (400) diffraction at 69.4° of the two Cu-K$_{\alpha}$ radiations. In addition, a peak at 61.8° is visible which can be assigned to the (400) diffraction of Cu-K$_{\beta}$ radiation from silicon [37].
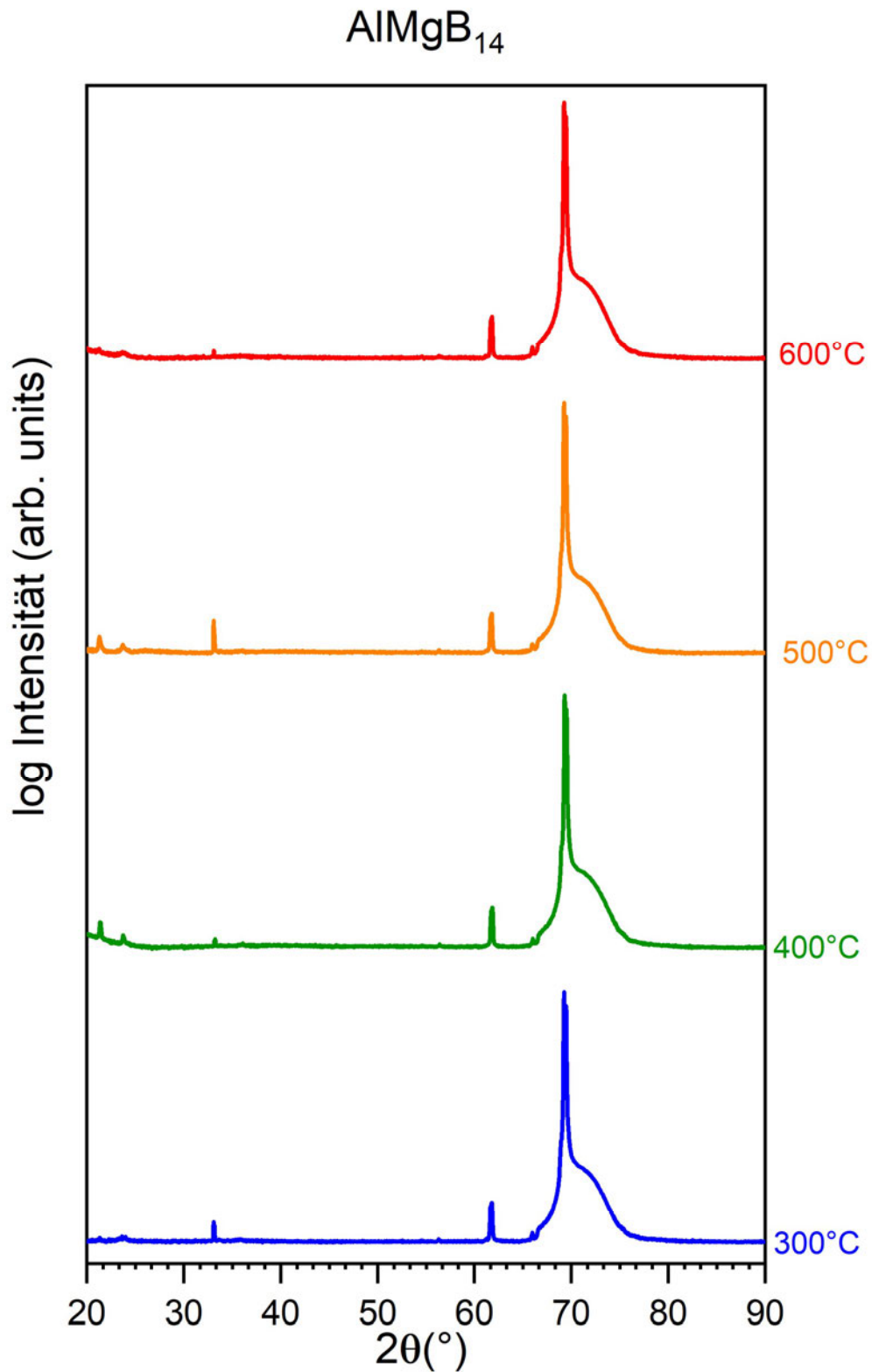
Figure 14: X-Ray diffraction pattern of ceramic AlMgB₁₄ on silicon substrates for different substrate temperatures from below 300 °C to above 600 °C

3.1.2 Annealed films

After researching existing publications [16]–[18], [38]–[42], the paper by V.I. Ivanshchenko [43] in particular pointed out that the amorphous structure begins to change in the range of 1000 °C annealing temperature. This was the reason for carrying out annealing tests of AlMgB$_{14}$ on sapphire substrate with annealing temperatures of 850, 900, 950, 1000, and 1050 °C with an annealing time of 20 min.
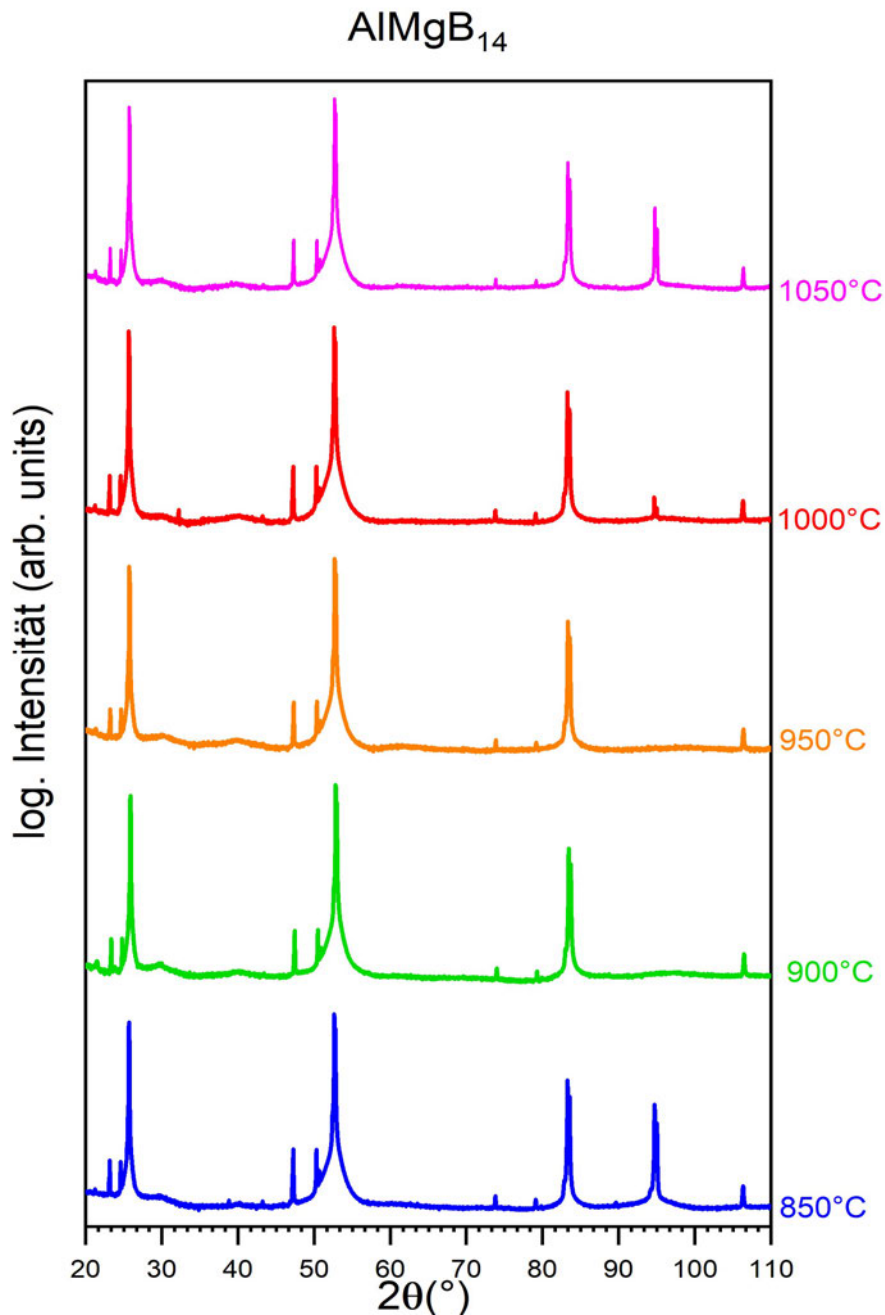

Figure 15: X-Ray diffraction pattern of ceramic AlMgB$_{14}$ on sapphire substrates for substrate temperatures of 600 °C and annealing temperature from bottom 850 °C to top 1050 °C

Comparing the measured XRD patterns of the different annealing tests (see Figure 15) with the reference pattern of the sapphire substrate (Figure 7), it can be seen that, essentially only the peaks of the substrate are present. The rather weak and wide XRD responses at 2θ-angles of around 30 and 40° may indicate the formation of nano-crystals but could be the response from the amorphous structure itself.

3.2 Mechanical Properties

3.2.1 Hardness of as-deposited films

In order to determine the influence of the substrate temperature during the deposition process on the hardness and the Young's modulus of the layer, nanoindentation measurements were carried out and evaluated.

For the $AlMgB_{14}$ coating on Sapphire substrates and a substrate temperature of 300 °C, the median values for the hardness and Young's modulus were 29.2 GPa and 372 GPa or a mean value of 29.3 GPa and 373 GPa with a standard deviation of 1.6 GPa and 17 GPa.

For the samples of the coating process with T_s = 400 °C, a hardness and a Young's modulus of 31.2 GPa and 294 GPa (both median values) and 31.0 ± 1.6 GPa and 389 ± 14 GPa were measured, respectively.

At the next higher substrate temperature (500 °C), the measured results were hardness of 32.6 ± 1.4 GPa (median: 33.0 GPa) and a Young's modulus of 409 ± 13 GPa (median: 409 GPa).

Finally, for the highest substrate temperature (600 °C), hardness values of 35.3 ± 1.0 GPa (median: 35.2 GPa) and Young's modulus of 413 ± 8 GPa (median: 414 GPa) were recorded.

The results of these measurements of the samples on sapphire substrates were visually illustrated in Figure 16.

For this purpose, the raw data of the measurement were converted into a graph using the Origin software and the statistical function "Box Chart". The values of the Young's modulus are shown in red and are read on the left axis and the hardness is shown in blue and is read on the right axis.

The representation of the graph should be understood as in Figure 17. The maximum and minimum values are shown with a cross, the top and bottom of the box represent the 75% limit and 25% limit of the measurements, the horizontal line in the box symbolises the median and the small square in the box the mean of the measurements and the 5% and 95% limits are shown with a short horizontal line. The median value is defined as a value so that 50% of the measurements with a low value are below it and 50% of the measurements with a value higher than it are above it. The mean is the sum of all the measurement results divided by the number of measurements.

It can be observed that both the hardness and the Young's modulus increase with increasing substrate temperature.
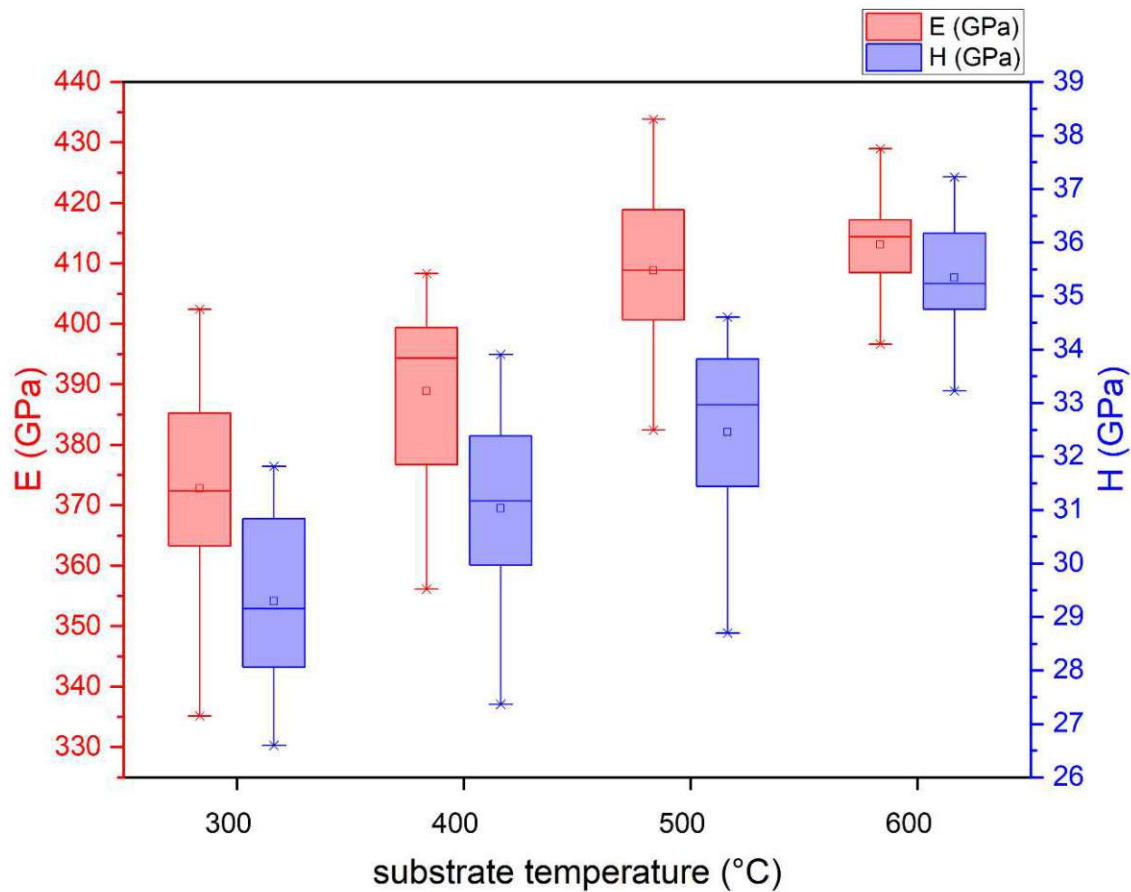
Figure 16: Hardness and Young's modulus of AlMgB$_{14}$ on sapphire substrates with T$_s$ from 300 °C to 600 °C
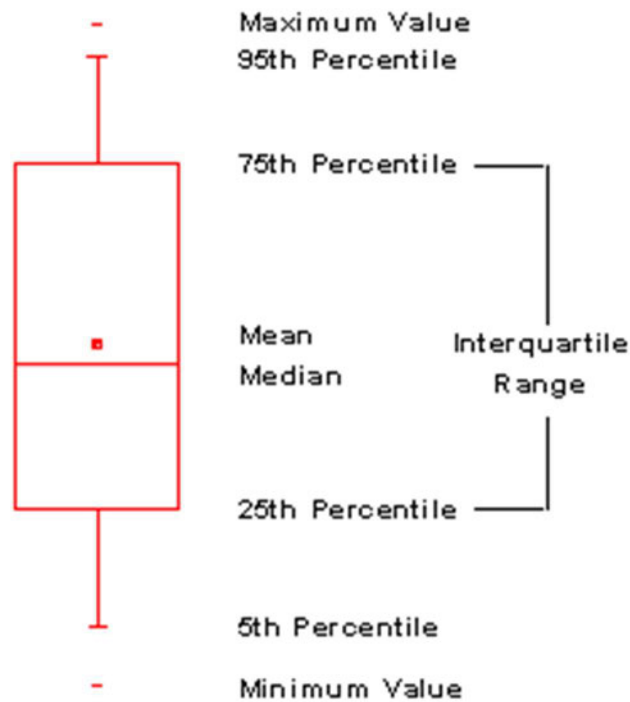
Figure 17: Explanation of the box chart from Origin [44]

3.2.2 Hardness of annealed films

After the annealing tests at 850 to 1050 °C in 50-degree Celsius steps, it was found that the E-modulus increased by about 50 GPa and the hardness increased by about 1 GPa.

More precisely, the E-modulus and hardness after the 850 °C annealing test is equal to 457 ± 11 GPa and 36.7 ± 0.6 GPa, for 900 °C equal to 462 ± 14 GPa and 35.9 ± 1.0 GPa, for 950 °C equal to 467 ± 12 GPa and 36.3 ± 1.1 GPa, for 1000 °C equal to 469 ± 13 GPa and 35.7 ± 0.9 GPa, and for 1050 °C equal to 461 ± 17 GPa and 36.2 ± 1.5 GPa. Compared to the as deposited state, the indentation modulus increases significantly which might be caused by crystallization, see Figure 18. Although there are no distinct peaks visible in XRD – except for the weak and wide XRD responses at 2θ-angles of around 30 and 40°, as mentioned above, see Fig. 15 – the increase of the indentation modulus also suggests for the formation of nano-crystals or at least for a more compact amorphous structure. Comparing the results for the individual annealing temperatures, no significant difference or trend between them can be observed, indicating that either the temperature or the time are too low to promote crystallization. This behavior can also be proven by XRD as there is no distinct difference between the diffraction patterns obtained after annealing at different temperatures.

27

The results are summarized in Figure 18, again using the box chart function from Origin, as explained in the previous chapter. This result (almost no difference between the differently annealed samples) suggests that "only" the amorphous structure is slightly rearranged towards a more compact structure, which is already achieved at 850 °C. The nucleation process to form crystals would thus need more time or higher temperatures.
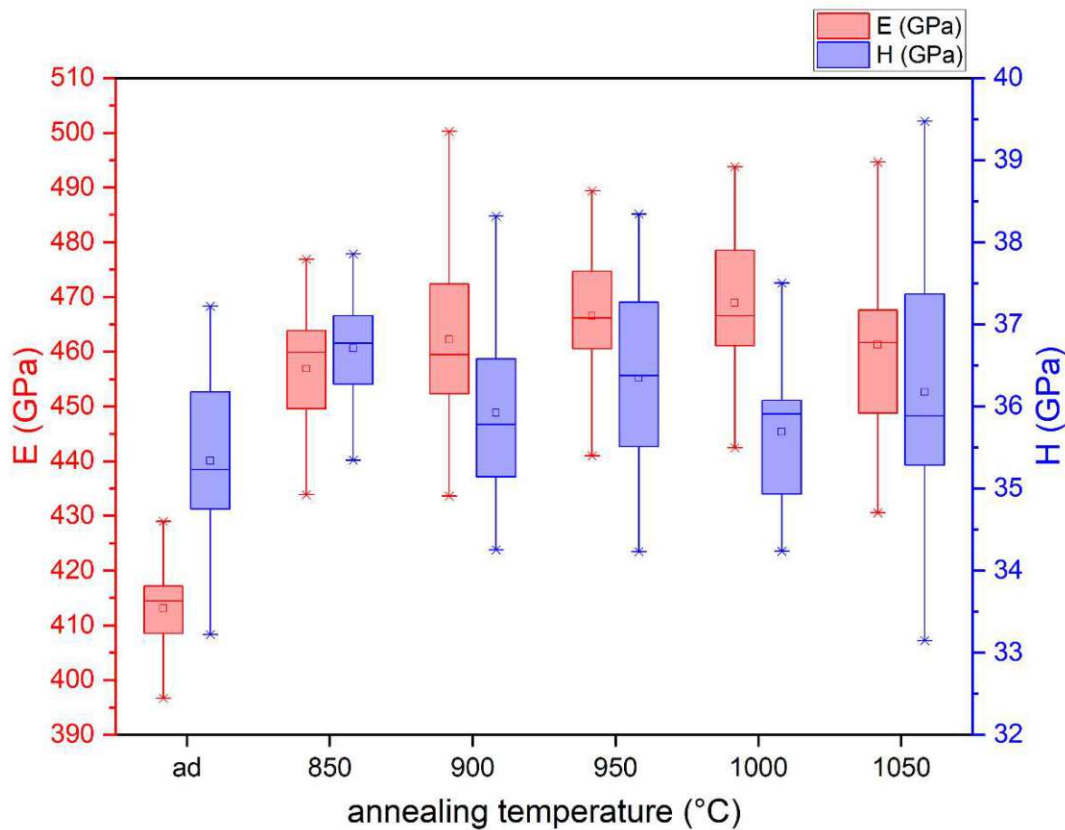
Figure 18: Hardness and Young's modulus of AlMgB$_{14}$ with T$_s$ = 600 °C after deposition, after annealing with 850 °C, 900 °C, 950 °C, 1000 °C, and 1050 °C

3.2.3 Residual Stresses

After determining the curvature (at least three measurements) of the AlMgB$_{14}$-coated sapphire substrates using a profilometer, the residual stresses were calculated per substrate temperature using the Stoney equation [45] and then averaged.

The modified Stoney equation,

$$\sigma = \frac{E_S}{1-\nu} * \frac{D^2}{6Rd} \qquad (5)$$

where σ is the residual stresses, E_S is the modulus of elasticity of the substrate, ν is the Poisson number of the substrate, D is the substrate thickness, d is the thickness of the film and R is the bending radius.

This calculation gave a residual stress in the coating of -2.37 ± 0.03 GPa for substrate temperature 300 °C, a residual stress of -2.11 ± 0.08 GPa for T_s = 400 °C, a coating residual stress of -2.96 ± 0.068 GPa for T_s = 500 °C and a residual stress of -2.89 ± 0.02 GPa for 600 °C substrate temperature. These results are also shown graphically in Figure 19.

It can be observed that all the layers have compressive stresses, which are beneficial for a long tool life, in the range of -2 GPa to -3 GPa and thus can be considered as approximately equivalent. The substrate temperature itself seems to have no significant influence on the residual stresses of the coatings.
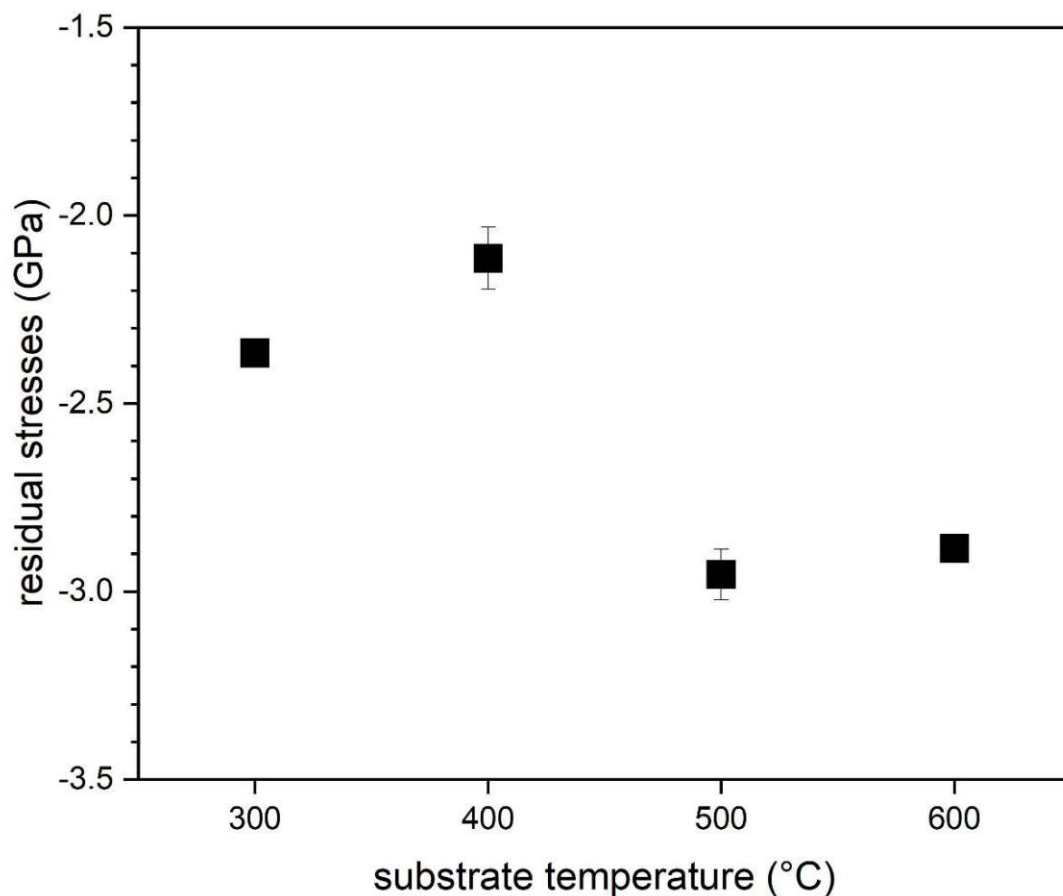

Figure 19: Residual stresses of AlMgB$_{14}$ coatings on sapphire substrates depending on the substrate temperature

3.2.4 Fracture Toughness

Fracture toughness (K_c) provides information on how well a brittle material resists cracking.

It states that the longer the crack length resulting from a cube-corner indenter measurement, the lower is the stress required to form the cracks or allow for their propagation. This means that a short crack results in a high fracture toughness, which is desirable, for example, for a long tool life. The unit of this quantity is MPa multiplied by the square root of m, which is to be equated with the unit of stress divided by the square root of the crack length. The formula (4) for this is given in chapter 2.3.4 cube-corner indentation [46]. After the samples are loaded with the cube corner tip and a defined force, images in the micrometre range can be taken with the FEGSEM equipment and the crack length can be measured, which is needed to calculate the fracture toughness. The arrangement of the, in total 15, measurement impressions for the sample produced with a substrate temperature of 600 °C is shown in Figure 20. In Fig. 21 the imprints are shown for a force of 250 mN and the samples with a substrate temperature of (a) 300 °C, (b) 400 °C, (c) 500 °C and (d) 600 °C.

Figure 20: Arrangement of the measurement impressions on AlMgB$_{14}$ (T$_s$ = 600 °C) with a force from 50 mN (left) to 450 mN (right)
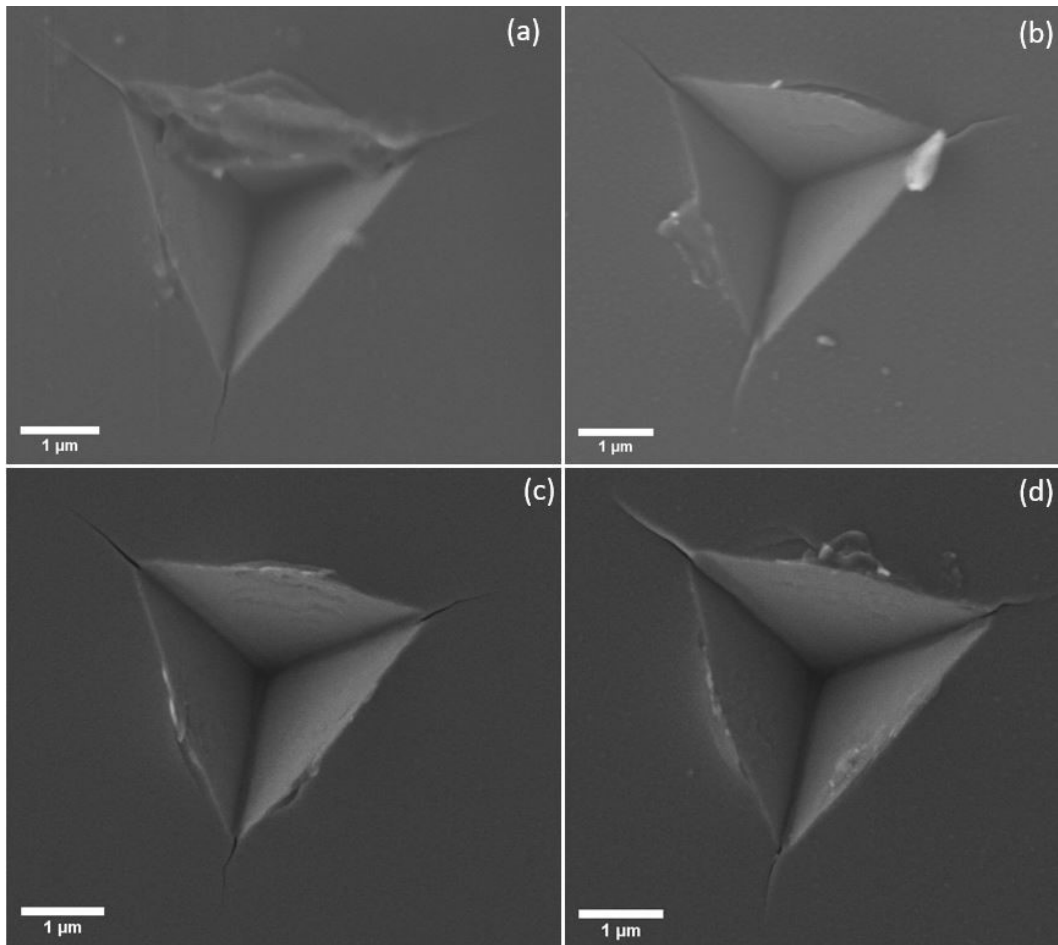
Figure 21: FEGSEM images of AlMgB$_{14}$ on sapphire substrate after a Cube-Corner indenter measurement with P = 250 mN with (a) 300 °C, (b) 400 °C, (c) 500 °C and (d) 600 °C substrate temperature

The calculation resulted in a fracture toughness of 3.72 ± 0.46 MPa√m, 4.43 ± 0.24 MPa√m, 4.98 ± 0.11 MPa√m, and 5.15 ± 0.22 MPa√m for an applied force of 250 mN for the substrate temperatures 300, 400, 500, and 600 °C, all measured and used data are summarised in Table 1.

It can be observed that with increasing substrate temperature, the fracture toughness also increases, see Figure 22. This trend is not so clear for the other measurements (50 mN, 150 mN, 350 mN and 450 mN), which is due to the large variation in the results and can be improved with an increase in the number of measurements at the same force.

In this chapter only the results for a force of 250 mN have been discussed, the results and pictures of all forces (50 mN, 150 mN, 250 mN, 350 mN, and 450 mN) are shown in the appendix.
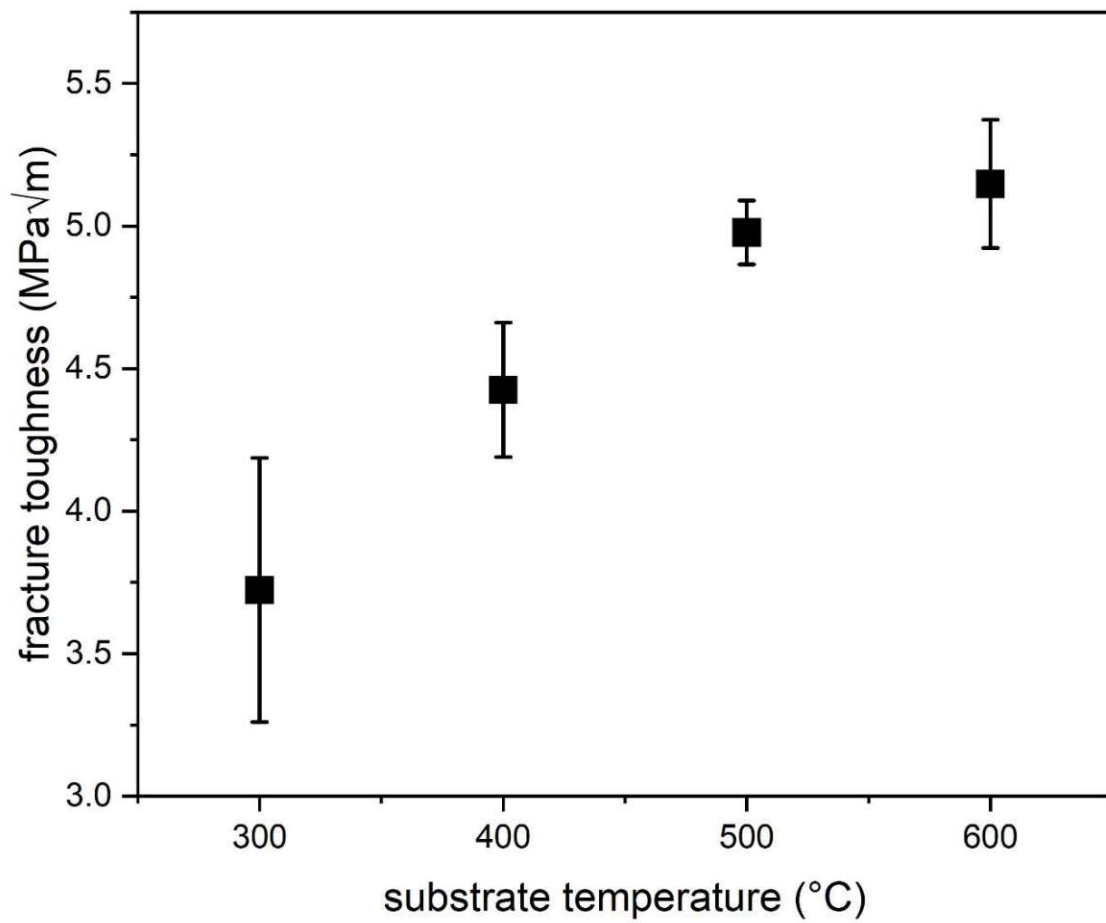
Figure 22: Fracture toughness with P = 250 mN of AlMgB$_{14}$ on sapphire substrates T$_s$ = 300 - 600 °C

Table 1: Fracture toughness with P = 250 mN of AlMgB$_{14}$ on sapphire substrates for several substrate temperatures (300 °C – 600 °C)

Substrate-temperature T_s	Young's Modulus E	Hardness H	crack length c	Alpha α	Force P	Fracture toughness K_c	Mean value K_c	standard deviation
°C	GPa	GPa	μm		mN	MPaVm	MPaVm	MPaVm
300	281	29.2	3.708	0.032	250	3.476	3.72	0.46
	281	29.2	3.822		250	3.321		
	281	29.2	3.182		250	4.372		
400	293	31.2	3.087	0.032	250	4.521	4.43	0.24
	293	31.2	3.027		250	4.655		
	293	31.2	3.294		250	4.101		
500	300	33	2.809	0.032	250	5.123	4.98	0.11
	300	33	2.872		250	4.956		
	300	33	2.913		250	4.852		
600	305	32.9	2.747	0.032	250	5.350	5.15	0.22
	305	32.9	2.939		250	4.834		
	305	32.9	2.779		250	5.258		

4 Conclusions and Outlook

AlMgB$_{14}$ coatings have been prepared by non-reactive magnetron sputtering of the respective 3-inch compound target. The four different films (3.1–3.6 µm thick, with growth rates of 52–60 nm/min) were prepared at four substrate temperatures (T_s) of 300, 400, 500, and 600 °C (with floating potential of the substrates). Their growth morphology is featureless and also the X-ray diffraction studies indicate a fully amorphous structure.

During the indentation of the AlMgB$_{14}$ coatings, rather high hardness values were found, which even increase with increasing substrate temperature. More precisely, the hardness value increases from 29.3 ± 1.6 GPa for T_s = 300 °C to 35.3 ± 1.0 GPa for T_s = 600 °C. Also, the Young's modulus increases from 373 ± 17 GPa (T_s = 300 °C) to 413 ± 8 GPa (T_s = 600 °C). Furthermore, independent on the substrate temperature, residual compressive stresses in the range from -2 to -3 GPa are present in the as-deposited films, which is desirable in principle. The fracture toughness also depends on the substrate temperature like the hardness and increases from 3.72 ± 0.46 to 5.15 ± 0.22 MPa√m with increasing T_s from 300 to 600 °C, respectively.

Regardless of their amorphous structure, the films exhibit very good mechanical properties. Vacuum annealing for 20 min at temperatures between 850 and 1050 °C only had a minor impact on the amorphous structure, as suggested by X-ray diffraction. In course of the various annealing treatments the hardness increased by about 1 GPa and the Young's modulus increased by approximately 50 GPa. As the various annealing temperatures resulted in the same hardness and Young's modulus increase, the formation of a more compact amorphous structure is more likely than the formation of nanocrystals during the annealing experiments.

Further investigations thus could concentrate on in-situ high-temperature XRD or transmission electron microscopy studies.

References

[1]   M. Ohring, *Materials science of thin films: depositon & structure*. Elsevier, 2001.

[2]   D. M. Mattox, *Handbook of physical vapor deposition (PVD) processing*. William Andrew, 2010.

[3]   W. S. Williams, „Transition metal carbides, nitrides, and borides for electronic applications", *Jom*, Bd. 49, Nr. 3, S. 38–42, 1997.

[4]   P. H. Mayrhofer *u. a.*, „Self-organized nanostructures in the Ti–Al–N system", *Appl. Phys. Lett.*, Bd. 83, Nr. 10, S. 2049–2051, 2003.

[5]   C. M. Koller *u. a.*, „Structure and mechanical properties of architecturally designed Ti-Al-N and Ti-Al-Ta-N-based multilayers", *Surf. Coat. Technol.*, Bd. 385, S. 125355, März 2020, doi: 10.1016/j.surfcoat.2020.125355.

[6]   R. Rachbauer, D. Holec, und P. H. Mayrhofer, „Phase stability and decomposition products of Ti–Al–Ta–N thin films", *Appl. Phys. Lett.*, Bd. 97, Nr. 15, S. 151901, 2010.

[7]   I.-W. Park, D. S. Kang, J. J. Moore, S. C. Kwon, J. J. Rha, und K. H. Kim, „Microstructures, mechanical properties, and tribological behaviors of Cr–Al–N, Cr–Si–N, and Cr–Al–Si–N coatings by a hybrid coating system", *Surf. Coat. Technol.*, Bd. 201, Nr. 9–11, S. 5223–5227, 2007.

[8]   A. Kirnbauer, C. Spadt, C. M. Koller, S. Kolozsvári, und P. H. Mayrhofer, „High-entropy oxide thin films based on Al–Cr–Nb–Ta–Ti", *Vacuum*, Bd. 168, S. 108850, Okt. 2019, doi: 10.1016/j.vacuum.2019.108850.

[9]   P. H. Mayrhofer, A. Kirnbauer, Ph. Ertelthaler, und C. M. Koller, „High-entropy ceramic thin films; A case study on transition metal diborides", *Scr. Mater.*, Bd. 149, S. 93–97, Mai 2018, doi: 10.1016/j.scriptamat.2018.02.008.

[10]   J.-W. YEH und A. DAVISON, „High-entropy alloys", 2006, Bd. 31, Nr. 6.

[11]   A. Kirnbauer *u. a.*, „Mechanical properties and thermal stability of reactively sputtered multi-principal-metal Hf-Ta-Ti-V-Zr nitrides", *Surf. Coat. Technol.*, Bd. 389, S. 125674, Mai 2020, doi: 10.1016/j.surfcoat.2020.125674.

[12]   V. I. Matkovich und J. Economy, „Structure of MgAlB$\sb 14$ and a brief critique of structural relationships in higher borides", *Acta Crystallogr. Sect. B*, Bd. 26, Nr. 5, S. 616–621, Mai 1970, doi: 10.1107/S0567740870002868.

[13]   Y. Tian *u. a.*, „Microstructure evolution of Al–Mg–B thin films by thermal annealing",

J. Vac. Sci. Technol. A, Bd. 21, Nr. 4, S. 1055–1063, Juli 2003, doi: 10.1116/1.1586274.

[14]   A. M. Grishin, „Abrasion resistant low friction and ultra-hard magnetron sputtered AlMgB14coatings", *Mater. Res. Express*, Bd. 3, Nr. 4, S. 046402, Apr. 2016, doi: 10.1088/2053-1591/3/4/046402.

[15]   A. Russell, B. Cook, J. Harringa, und T. Lewis, „Coefficient of thermal expansion of AlMgB 14", *Scr. Mater. - Scr. MATER*, Bd. 46, S. 629–633, Mai 2002, doi: 10.1016/S1359-6462(02)00034-9.

[16]   A. M. Grishin, „Hardness, young's modulus and elastic recovery in magnetron sputtered amorphous AlMgB14 films", *Crystals*, Bd. 10, Nr. 9, S. 823, 2020.

[17]   M. Noroozi, A. Petruhins, G. Greczynski, J. Rosen, und P. Eklund, „Structural and mechanical properties of amorphous AlMgB14 thin films deposited by DC magnetron sputtering on Si, Al2O3 and MgO substrates", *Appl. Phys. A*, Bd. 126, Nr. 2, S. 1–6, 2020.

[18]   A. Grishin, S. Khartsev, J. Böhlmark, und M. Ahlgren, „Ultra-hard AlMgB14 coatings fabricated by RF magnetron sputtering from a stoichiometric target", *JETP Lett.*, Bd. 100, Nr. 10, S. 680–687, 2015.

[19]   J. C. Britson, *Pulsed laser deposition of aluminum magnesium borate thin films*. Iowa State University, 2008.

[20]   W. D. Westwood, „Sputter deposition", 2003.

[21]   P. H. Mayrhofer, „Surface Technology", TU Wien, Summer term 2020.

[22]   7_B A Movchan und A. Demchishin, „STRUCTURE AND PROPERTIES OF THICK CONDENSATES OF NICKEL, TITANIUM, TUNGSTEN, ALUMINUM OXIDES, AND ZIRCONIUM DIOXIDE IN VACUUM.", *Fiz Met. Met. 28 653-60 Oct 1969*, 1969.

[23]   J. A. Thornton, „High rate thick film growth", *Annu. Rev. Mater. Sci.*, Bd. 7, Nr. 1, S. 239–260, 1977.

[24]   R. Messier, A. Giri, und R. Roy, „Revised structure zone model for thin film physical structure", *J. Vac. Sci. Technol. Vac. Surf. Films*, Bd. 2, Nr. 2, S. 500–503, 1984.

[25]   A. Anders, „A structure zone diagram including plasma-based deposition and ion etching", *Thin Solid Films*, Bd. 518, Nr. 15, S. 4087–4090, 2010.

[26]   J. Fuerst, M. Carter, und J. Sears, „LASER POWDER DEPOSITION OF ALMGB14-TIB2 ULTRA-HARD COATINGS ON TITANIUM, AND STEEL SUBSTRATES", *Suppl. Proc. Mater. Process. Interfaces*, Bd. 1, S. 561–568, 2012.

[27]   W. L. Bragg, „The diffraction of short electromagnetic waves by a crystal", *Scientia*,

Bd. 23, Nr. 45, 1929.

[28]   E. Halwax, „A very short introductory course on the diffraction of X-rays from polycrystalline samples", TU Wien, 2022.

[29]   M. De Graef, Hrsg., „Basic quantum mechanics, Bragg's Law and other tools", in *Introduction to Conventional Transmission Electron Microscopy*, Cambridge: Cambridge University Press, 2003, S. 79–135. doi: 10.1017/CBO9780511615092.004.

[30]   W. C. Oliver und G. M. Pharr, „An improved technique for determining hardness and elastic modulus using load and displacement sensing indentation experiments", *J. Mater. Res.*, Bd. 7, Nr. 6, S. 1564–1583, 1992.

[31]   G. Pharr, „Measurement of mechanical properties by ultra-low load indentation", *Mater. Sci. Eng. A*, Bd. 253, Nr. 1–2, S. 151–159, 1998.

[32]   B. R. Lawn, A. G. Evans, und D. Marshall, „Elastic/plastic indentation damage in ceramics: the median/radial crack system", *J. Am. Ceram. Soc.*, Bd. 63, Nr. 9-10, S. 574–581, 1980.

[33]   J. Kruzic, D. Kim, K. Koester, und R. Ritchie, „Indentation techniques for evaluating the fracture toughness of biomaterials and hard tissues", *J. Mech. Behav. Biomed. Mater.*, Bd. 2, Nr. 4, S. 384–395, 2009.

[34]   J. I. Goldstein, D. Newbury, J. Michael, und N. Ritchie, „J. Henry J. Scott, Joy DC Scanning Electron Microscopy and X-Ray Microanalysis", 2017.

[35]   C. Sciammarella *u. a.*, „Measurements of Deflection and Residual Stress in Thin Films Utilizing Coherent Light Reflection/Projection Moiré Interferometry", *Exp. Mech.*, Bd. 53, Nr. 6, S. 977–987, 2013.

[36]   V. Siderov *u. a.*, „Film thickness measurement by optical profilometer MicroProf® FRT", *Bulg. Chem. Commun.*, Bd. 45, S. 194–197, 2013.

[37]   K. Okamura, B. Nasr, R. A. Brand, und H. Hahn, „Solution-processed oxide semiconductor SnO in p-channel thin-film transistors", *J. Mater. Chem.*, Bd. 22, Nr. 11, S. 4607–4610, 2012.

[38]   Z. Wu *u. a.*, „Al–Mg–B thin films prepared by magnetron sputtering", *Vacuum*, Bd. 85, Nr. 4, S. 541–545, 2010.

[39]   D. Nesmelov, S. Perevislov, D. Danilovich, N. Khristyuk, und S. Ordan'yan, „On the Melting Point of AlMgB14", *Glass Phys. Chem.*, Bd. 45, Nr. 4, S. 305–307, 2019.

[40]   V. Putrolaynen, A. M. Grishin, und I. Rigoev, „Anti-Scratch AlMgB14 Gorilla® Glass

Coating", *Tech. Phys. Lett.*, Bd. 43, Nr. 10, S. 871–874, 2017.

[41]   M. Yuzvyuk, V. Putrolaynen, und A. M. Grishin, „Processing of ultra-hard coatings based on AlMgB14 films", 2016, Bd. 769, Nr. 1, S. 012039.

[42]   B. A. Cook, Y. Tian, J. L. Harringa, A. P. Constant, A. M. Russell, und P. A. Molian, „Ultra-hard low friction coating based on A1MgB14 for reduced wear of MEMS and other tribological components and system", Juli 2007.

[43]   V. Ivashchenko, P. Scrynskyy, S. Dub, O. Butenko, A. Kozak, und O. Sinelnichenko, „Structural and mechanical properties of Al—Mg—B films: Experimental study and first-principles calculations", *Thin Solid Films*, Bd. 599, S. 72–77, 2016.

[44]   „Help   Online   -   Origin   Help   -   Creating   Box   Charts". https://www.originlab.com/doc/origin-help/create-box-chart (zugegriffen 29. Juni 2022).

[45]   P. A. Flinn, D. S. Gardner, und W. D. Nix, „Measurement and interpretation of stress in aluminum-based metallization as a function of thermal history", *IEEE Trans. Electron Devices*, Bd. 34, Nr. 3, S. 689–699, 1987.

[46]   A. Vaidya und K. Pathak, „Mechanical stability of dental materials", in *Applications of Nanocomposite Materials in Dentistry*, Elsevier, 2019, S. 285–305.

Appendix

Cube Corner Indents

FEGSEM - images of cube corner indentation with a force 50 mN, 250 mN, 150 mN, 350 mN and 450 mN are listed in this chapter.
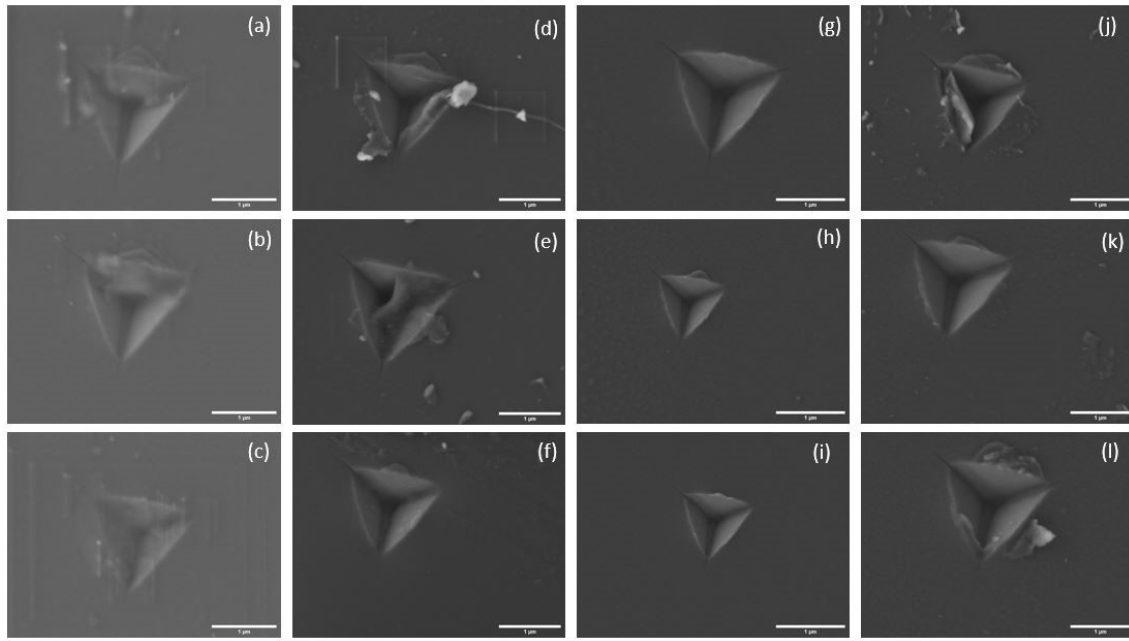
Figure A 1: Cube corner indents with P = 50mN on AlMgB$_{14}$ with T$_s$ = 300 °C (a)-(c), T$_s$ = 400 °C (d)-(f), T$_s$ = 500 °C (g)-(i) and T$_s$ = 600 °C (j)-(l)
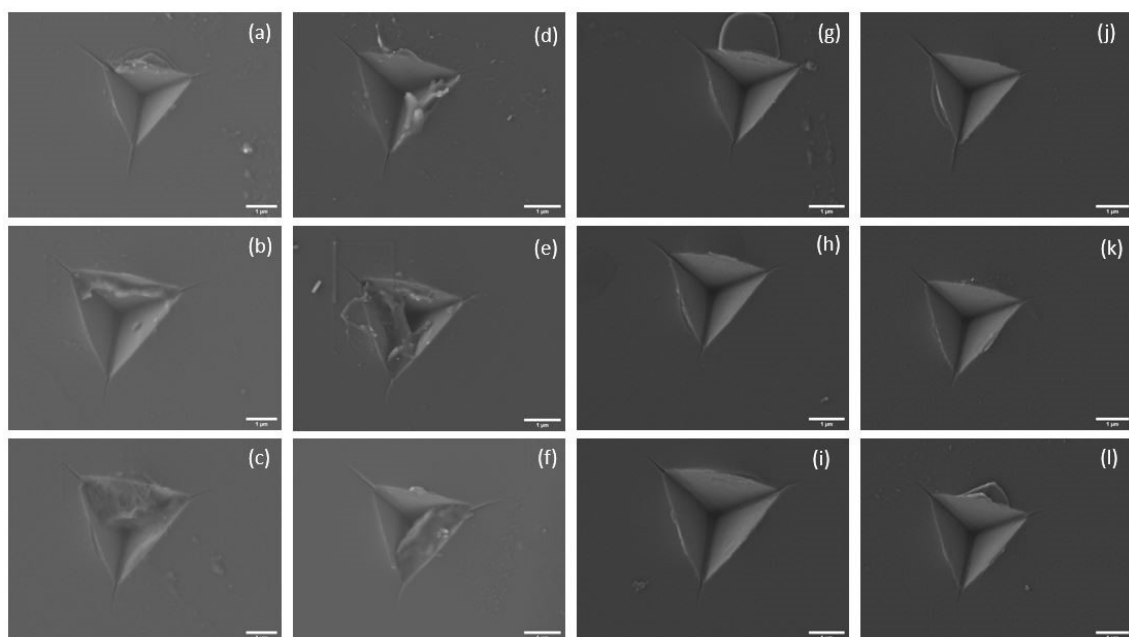
Figure A 2: Cube corner indents with P = 150 mN on AlMgB$_{14}$ with T$_s$ = 300 °C (a)-(c), T$_s$ = 400 °C (d)-(f), T$_s$ = 500 °C (g)-(i) and T$_s$ = 600 °C (j)-(l)
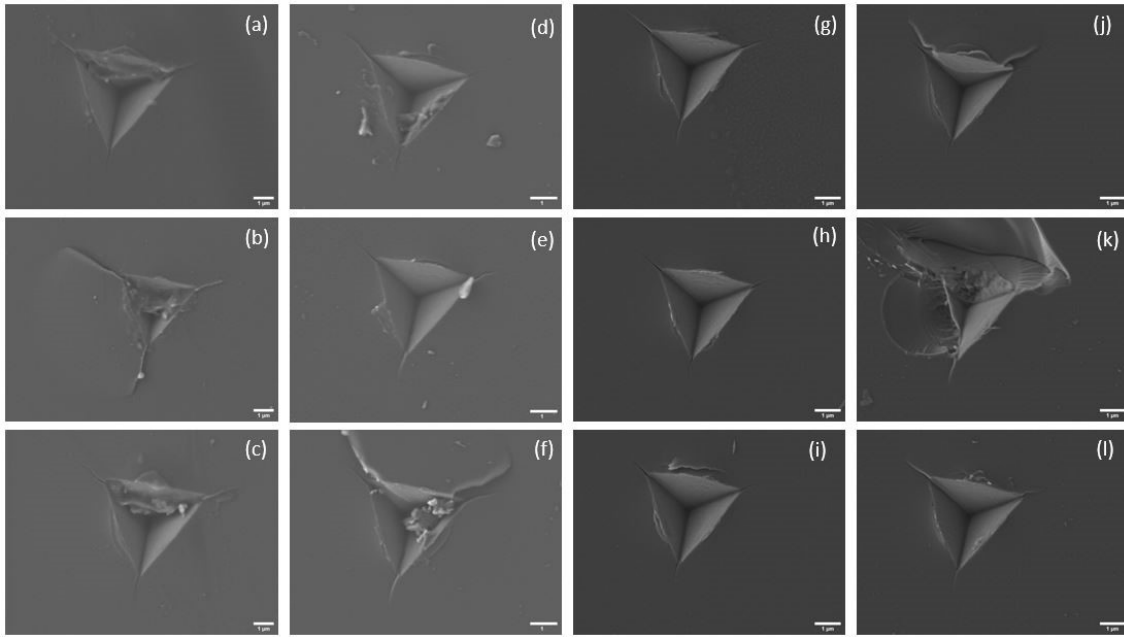
Figure A 3: Cube corner indents with P = 250 mN on AlMgB$_{14}$ with T$_s$ = 300 °C (a)-(c), T$_s$ = 400 °C (d)-(f), T$_s$ = 500 °C (g)-(i) and T$_s$ = 600 °C (j)-(l)
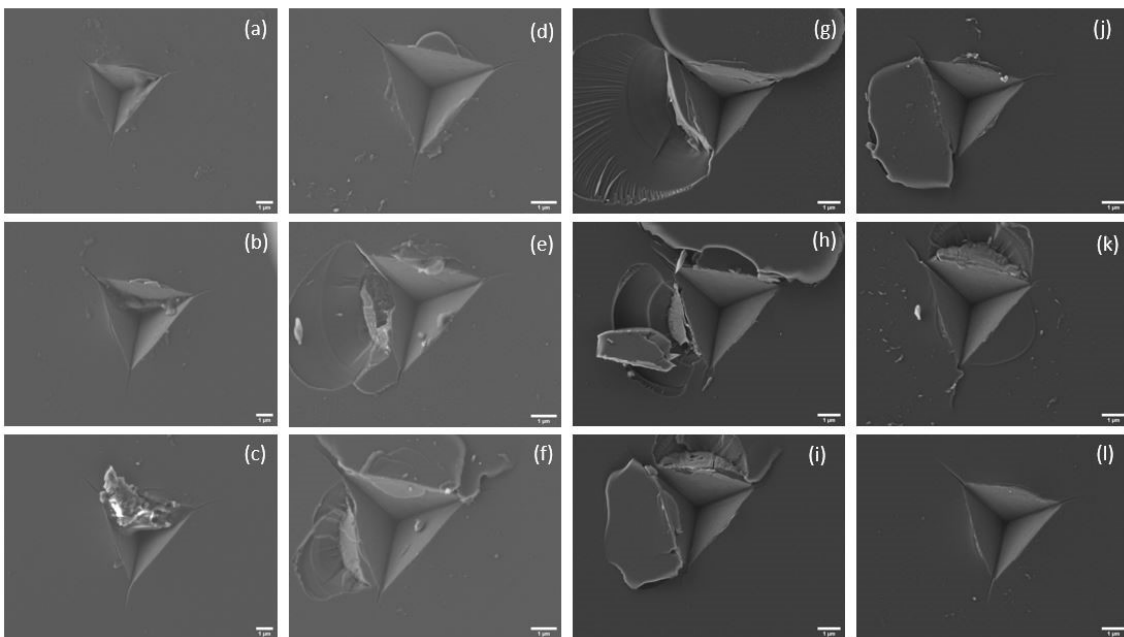
Figure A 4: Cube corner indents with P = 350 mN on AlMgB$_{14}$ with T$_s$ = 300 °C (a)-(c), T$_s$ = 400 °C (d)-(f), T$_s$ = 500°C (g)-(i) and T$_s$ = 600°C (j)-(l)

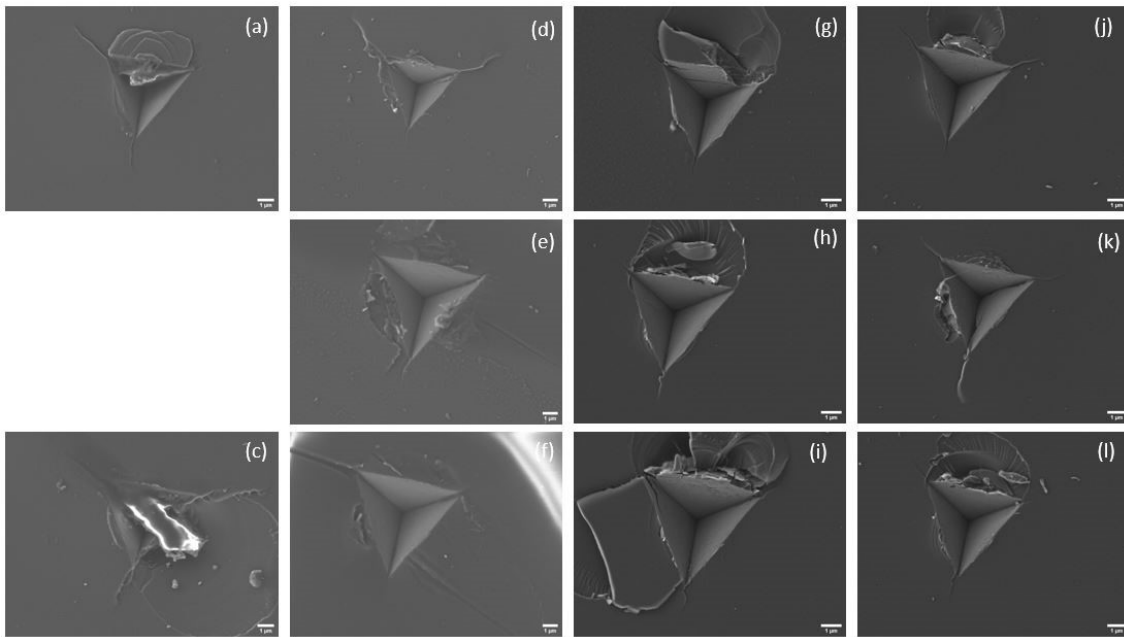*Figure A 5: Cube corner indents with P = 450 mN on AlMgB$_{14}$ with T$_s$ = 300 °C (a, c), T$_s$ = 400 °C (d)-(f), T$_s$ = 500°C (g)-(i) and T$_s$ = 600°C (j)-(l)*

On the next three pages, all measured values and results of the fracture toughness are listed in tabular form for 50 mN to 450 mN.

Table A 1: Values for calculating the fracture toughness of AlMgB₁₄ and the results for a force of 50 mN

Substrate-temperature T_s	Young's Modulus E	Hardness H	Substrat	crack length c	Alpha α	Force P	Fracture toughness K_c	Mean value K_c	standard deviation
°C	GPa	GPa		μm		mN	MPa√m	MPa√m	MPa√m
300	281	29.2	Sapphire	1.280	0.032	50	3.427	3.42	0.01
	281	29.2		1.285		50	3.407		
	281	29.2				50			
400	293	31.2	Sapphire	1.260	0.032	50	3.467	3.37	0.20
	293	31.2		1.359		50	3.095		
	293	31.2		1.239		50	3.555		
500	300	33	Sapphire	1.188	0.032	50	3.726	3.60	0.14
	300	33		1.200		50	3.670		
	300	33		1.264		50	3.395		
600	305	32.9	Sapphire	1.212	0.032	50	3.651	3.92	0.22
	305	32.9		1.156		50	3.920		
	305	32.9		1.106		50	4.188		

Table A 2: Values for calculating the fracture toughness of AlMgB₁₄ and the results for a force of 150 mN

Substrate-temperature T_s	Young's Modulus E	Hardness H	Substrat	crack length c	Alpha α	Force P	Fracture toughness K_c	Mean value K_c	standard deviation
°C	GPa	GPa		μm		mN	MPa√m	MPa√m	MPa√m
300	281	29.2	Sapphire	2.402	0.032	150	4.000	4.03	0.04
	281	29.2		2.404		150	3.995		
	281	29.2		2.368		150	4.086		
400	293	31.2	Sapphire	2.176	0.032	150	4.583	4.11	0.43
	293	31.2		2.301		150	4.213		
	293	31.2		2.588		150	3.533		
500	300	33	Sapphire	2.202	0.032	150	4.429	4.54	0.15
	300	33		2.196		150	4.447		
	300	33		2.102		150	4.749		
600	305	32.9	Sapphire	2.130	0.032	150	4.701	4.95	0.17
	305	32.9		2.034		150	5.038		
	305	32.9		2.018		150	5.098		

Table A 3: Values for calculating the fracture toughness of AlMgB14 and the results for a force of 350 mN

Substrate-temperature T_s	Young's Modulus E	Hardness H	Substrat	crack length c	Alpha α	Force P	Fracture toughness K_c	Mean value K_c	standard deviation
°C	GPa	GPa		µm		mN	MPaVm	MPaVm	MPaVm
300	281	29.2	Sapphire	3.708	0.032	250	3.476	3.72	0.46
	281	29.2		3.822		250	3.321		
	281	29.2		3.182		250	4.372		
400	293	31.2	Sapphire	3.087	0.032	250	4.521	4.43	0.24
	293	31.2		3.027		250	4.655		
	293	31.2		3.294		250	4.101		
500	300	33	Sapphire	2.809	0.032	250	5.123	4.98	0.11
	300	33		2.872		250	4.956		
	300	33		2.913		250	4.852		
600	305	32.9	Sapphire	2.747	0.032	250	5.350	5.15	0.22
	305	32.9		2.939		250	4.834		
	305	32.9		2.779		250	5.258		

Table A 4: Values for calculating the fracture toughness of AlMgB$_{14}$ and the results for a force of 350 mN

Substrate-temperature T_s	Young's Modulus E	Hardness H	Substrat	crack length c	Alpha α	Force P	Fracture toughness K_c	Mean value K_c	standard deviation
°C	GPa	GPa		µm		mN	MPaVm	MPaVm	MPaVm
300	281	29.2	Sapphire	3.583	0.032	350	5.123	5.12	0.01
	281	29.2		3.576		350	5.138		
	281	29.2		3.588		350	5.112		
400	293	31.2	Sapphire	3.485	0.032	350	5.276	5.35	0.08
	293	31.2		3.405		350	5.463		
	293	31.2		3.472		350	5.304		
500	300	33	Sapphire		0.032	350		5.87	0.23
	300	33		3.296		350	5.643		
	300	33		3.128		350	6.106		
600	305	32.9	Sapphire	3.958	0.032	350	4.331	5.04	0.52
	305	32.9		3.355		350	5.550		
	305	32.9		3.487		350	5.237		

Table A 5: Values for calculating the fracture toughness of AlMgB$_{14}$ and the results for a force of 450 mN

Substrate-temperature T_s	Young's Modulus E	Hardness H	Substrat	crack length c	Alpha α	Force P	Fracture toughness K_c	Mean value K_c	standard deviation
°C	GPa	GPa		μm		mN	MPaVm	MPaVm	MPaVm
300	281	29.2	Sapphire	4.710	0.032	450	4.370	4.48	0.11
	281	29.2				450			
	281	29.2		4.554		450	4.597		
400	293	31.2	Sapphire	4.225	0.032	450	5.081	5.30	0.21
	293	31.2		4.003		450	5.510		
	293	31.2				450			
500	300	33	Sapphire	4.333	0.032	450	4.814	4.72	0.14
	300	33		4.319		450	4.837		
	300	33		4.519		450	4.520		
600	305	32.9	Sapphire	4.176	0.032	450	5.1378	5.12	0.27
	305	32.9		4.385		450	4.775		
	305	32.9		4.022		450	5.436		